I THE MODE LOCKED DYE LASER

II PICOSECOND PHOTOCONDUCTIVITY OF SEMI-INSULATING GALLIUM ARSENIDE

Thesis by

Richard H. Moyer

In Partial Fulfillment of the Requirements

for the Degree of

Doctor of Philosophy

California Institute of Technology

Pasadena, California

1980

(submitted April 29,1980)

To Paula

ACKNOWLEDGEMENTS

I wish to acknowledge the fine support given to me by a number of people. First, I would like to thank my thesis advisor Professor Amnon Yariv for his support and advice throughout this endeavor.

I am also very grateful to my colleagues in this project, Pinchas Agmon and Thomas Koch. I wish them good fortune in their careers.

Special thanks go to Desmond Armstrong whose highly competent technical assistance facilitated all the experimental work in this thesis.

My wife Paula deserves my greatest appreciation. Her confidence and love were an inspiration to my work.

ABSTRACT

The first part of this thesis deals with the principles and practice of the passive mode locking of a CW dye laser. This discussion includes the dynamics of picosecond pulse production as well as the techniques of high resolution pulse width measurement. The characterization of the mode locked dye laser through real-time temporal and spectral measurements is also described.

The second part of the thesis describes the development and applications of the opto-electronic semiconductor switch. Design considerations of the high speed photoconductive device and results of experiments in which picosecond pulses activate the devices are discussed. The experimental results are interpreted to yield numerical estimates of carrier recombination rates. A new experimental technique of determining these parameters through ultrafast magnetophotoconductivity is introduced as well. The results of this technique show good agreement with the steady state measurements.

FORWARD

Charles Shank and Eric Ippen developed the first passively mode locked CW dye laser at Bell Laboratories in 1974. This device produced subpicosecond optical pulses, which facilitated the measurement of extremely fast transient phenomena.

Caltech research in ultrafast semiconductor processes began in 1975 when Pinchas Agmon studied Ippen and Shank's laser in order to construct the laser and use it for picosecond spectroscopy in semiconductors. Agmon analyzed the physics of the seven mirror dye laser as well as the pulse width measurement system in operation at Bell Laboratories.

In 1976, I joined Agmon in the design and construction of the mode locked dye laser. Two years later, we had the capability of consistently generating picosecond pulses with our laser. During this time, we designed experiments for the study of the ultrafast photoconductivity of GaAs. By the end of Agmon's stay at Caltech, we had established the existence of surface effects in the operation of the optoelectronic switch.

In order to quantitatively delineate the surface and bulk effects in the optoelectronic switch, I performed the first ultrafast magnetophotoconductivity experiments. This technique allowed an accurate determination of the recombination parameters of GaAs, and established a deeper understanding of optoelectronic switching phenomena.

TABLE OF CONTENTS

PART I. THE MODE LOCKED DYE LASER

PART II. PICOSECOND PHOTOCONDUCTIVITY OF SEMI-INSULATING GALLIUM ARSENIDE

Chapter 1

The Mode Locked Laser

1.0 Introduction

The mode locked laser is an important source of short optical pulses for use in the investigation of transient phenomena. Since 1964, when Hargrove first demonstrated mode locking with a He-Ne laser[1], the pulse duration of mode locked lasers has dropped from a few nanoseconds to 0.2 picoseconds. A result of this dramatic improvement in techniques and devices has been the measurement of ultrafast processes in organic compounds, nonlinear optical crystals, and semiconductors with subpicosecond temporal resolution.

Prior to the development of the mode locked dye laser, the shortest optical pulses were produced with the mode locked Nd:glass laser. This laser is capable of producing a burst of powerful (millijoule) subpicosecond pulses. It is necessary to extract a single pulse from this burst for use in experiments. The drawbacks of this system include the non-reproducibility of the pulses from burst to burst, and the difficulties of pulse extraction systems. In 1974, Ippen and Shank developed the mode locked dye laser [2,3]. This device produces

a continuous train of subpicosecond nanojoule pulses with a high degree of reproducibility. These features allow convenient, low-noise data acquisition with exceedingly high temporal resolution. Subsequently, Ippen and Shank developed an amplifier for the dye laser, increasing the output to millijoule pulses [4]. Thus, the mode locked dye laser became a choice instrument for use in picosecond spectroscopy of materials.

1.1 The Principles of Mode Locking

The electromagnetic field in a laser cavity can be approximated with a superposition of empty cavity modes:

$$E(t)=\sum_{n}^{N} E_n e^{i[\omega_0+n\pi\frac{c}{L}]t+i\varphi_n(t)} \qquad 1.1$$

where E_n is the electric field amplitude of the nth mode, φ_n is the phase of the nth mode, ω_0 is the center oscillating frequency, c is the speed of light, and L is the length of the cavity. N is the number of oscillating modes. In practice, these modes exhibit random relative phase; the superposition field will show statistical amplitude fluctuations specified by the random phases. Mode locking consists of fixing the relative phases of the lasing modes to some constant, or n times some constant. When this happens, the superposition field becomes

$$E(t)=e^{i[\omega_0 t+\varphi]}\frac{\sin(N\omega t/2)}{\sin(\omega t/2)} \qquad \omega \equiv \frac{c}{2L} \qquad 1.2$$

The optical power is proportional to the squared amplitude of the electric field:

$$P(t) \alpha \frac{\sin^2(N\omega t/2)}{\sin^2(\omega t/2)} \qquad 1.3$$

Thus, in this approximation, the output of a mode locked laser is a train of pulses separated in time by 2L/c, which is the cavity round trip time, and each pulse has a width of $1/\Delta\nu$ which is the inverse lasing bandwidth[5a].

1.2 Mode Locking Techniques

There are two basic means of mode locking a laser: actively and passively. A laser is actively mode locked when the gain (or loss) or the dispersion in the cavity is modulated, usually at the round trip cavity frequency, by some external driver. Passive mode locking occurs when a substance or device is present in the cavity, and the natural dispersive or absorptive effect of the introduced system locks the modes of the laser.

Active mode locking requires the insertion of an element in the laser cavity capable of modulating its gain, loss, or dispersion. This is commonly done acousto-optically or electro-optically. Another method of active mode locking, particularly relevant to

the discussion of the mode locked dye laser, is the synchronous pumping of one laser by a mode locked master laser. One of the most notable demonstrations of this technique has been the synchronous pumping of a dye laser by a mode locked argon laser. The advantage of this approach is a great simplification in the design of the dye laser (since there is no need for a saturable absorber) with only a moderate sacrifice in pulse width (0.8 psec instead of 0.2 psec).

Passive mode locking with a dispersive medium can be achieved with a substance possessing a non-zero Kerr coefficient. Each pair of adjacent Fabry-Perot modes of the cavity is mixed by the non-linear effect of the Kerr medium, producing a polarization oscillating at the beat frequency. This polarization modulates each cavity mode, coupling it coherently with the two adjacent modes. The result of this and all higher order effects will be to lock the phases of the lasing modes[6].

Passive mode locking with an absorbing medium is typically done with a saturable absorber. This technique is the one used to mode lock the dye laser described in the first part of this thesis. Saturable absorbers have the general property that their transmissivities increase with increasing incident intensity (Figure 1.1). The effect of such absorbers on a laser is most conveniently approached in the time domain. In the case of the mode locked dye

laser, there are many (10,000) modes lasing simultaneously. As stated above, these modes, if left alone, would oscillate in random relative phase; the total laser intensity would thus fluctuate randomly about a mean value. Assume that the gain of the laser is set so that this mean intensity is on the order of the saturation intensity of the absorber (Figure 1.2). Fluctuations that exceed the saturation intensity will experience less attenuation than those below. After one round trip through the cavity, the highest peaks survive, and the smaller peaks are lost. There will always be one largest peak in the fluctuations; this peak will be least attenuated, and the others will be correspondingly more absorbed. In the steady state, this one largest pulse will prevail.

From the above argument, one might conclude that the one surviving pulse would have a width equal to the relaxation time of the saturable absorber. Such relaxation times are on the order of 10-100 picoseconds. Experimentally, pulses much shorter than this limit are observed with durations of less than 1 picosecond. The explanation for this phenomenon is that the pulse is shaped by two agents: the saturable amplifier as well as the saturable absorber. Figure 1.3 demonstrates the action of these two saturable media on a broad pulse. When the pulse reaches the saturable absorber, it expends a portion of its leading edge to saturate the medium. This shortens the risetime of the pulse. When the pulse is amplified by

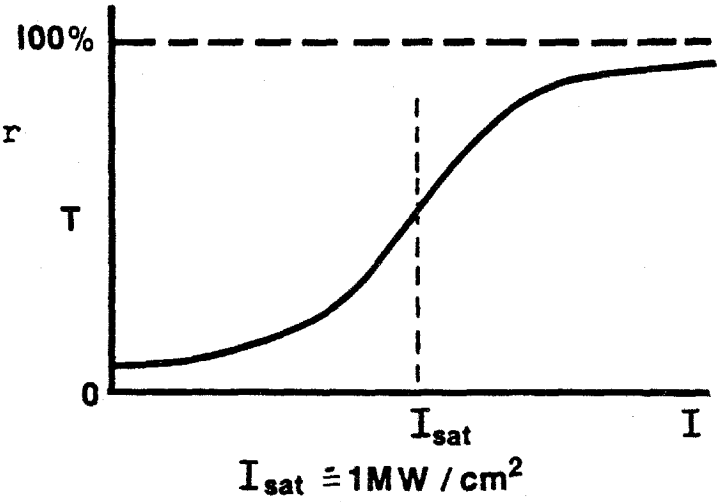

Figure 1.1
Transmission curve of a saturable absorber as a function of incident intensity

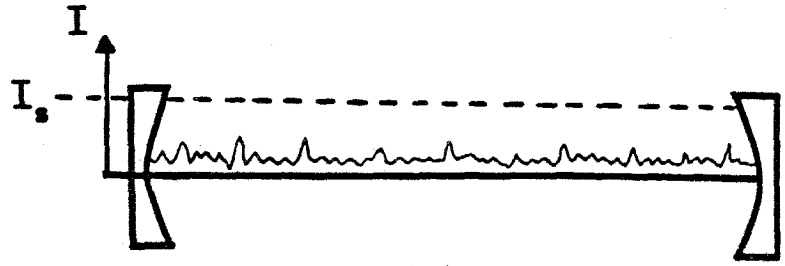

(a)
Initially

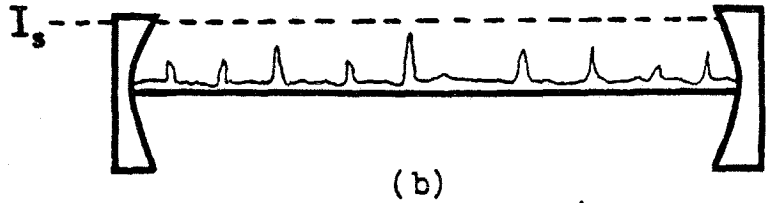

(b)
After one round trip

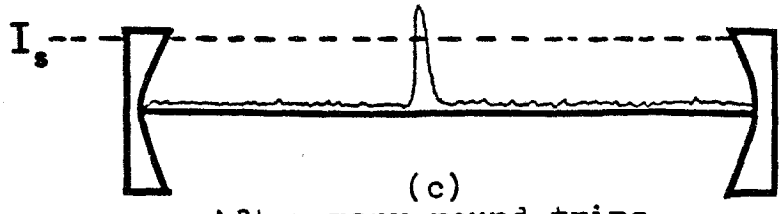

(c)
After many round trips

Figure 1.2
The effect of a saturable absorber upon the intercavity laser energy

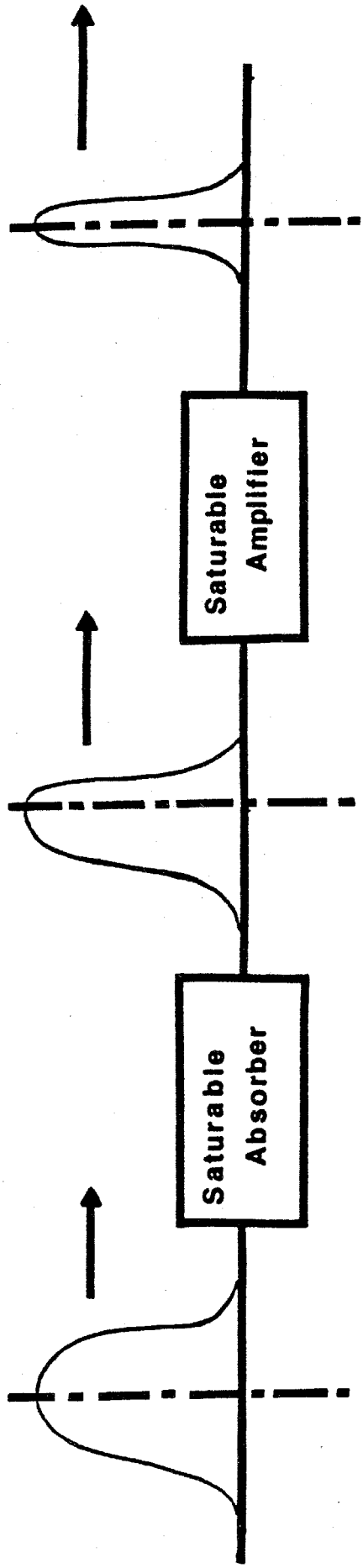

Figure 1.3 The narrowing of a picosecond pulse through non-linear intercavity media.

the gain medium, the first part of the pulse depletes the inversion of the amplifier. The remainder of the pulse experiences less amplification or even attenuation, with the result that the fall time of the pulse is reduced as well. The steady state pulsewidth, therefore, can be considerably shorter than the relaxation time of the lasing or absorbing media. Exhaustive theoretical studies of this process have been done by Haus and Ausschnitt [7,8].

Chapter 2

The Passively Mode Locked CW Dye Laser

2.0 Introduction

After Ippen and Shank developed a CW (continuous wave) dye laser in 1970, there were many attempts to mode lock similarly constructed dye lasers. The technology of ultra-stable oscillators had not yet developed to the degree required (stabilities of 10Hz in 100Mhz) to promote the development of synchronously pumped systems. The alternative was to use saturable absorbers, a technique already in a mature stage of application to pulsed mode locked lasers, such as the Nd:Yag and Nd:glass lasers.

Various cavity configurations and saturable absorbers were used in attempts to mode lock the CW dye laser. The best passively mode locked system in terms of pulse stability, pulse power, and pulse width was the apparatus demonstrated by Ippen and Shank [3]. Their laser was a seven mirror twin dye-jet system with an acousto-optic output coupler (See Figure 2.3). This device produced 0.3 picosecond kilowatt pulses at 610 nm. We undertook the task of deriving the understanding of its behavior in order to design and construct the system in our laboratory for study of ultrafast phenomena in semiconductors and semiconductor devices.

2.1 General Properties of Dyes

The use of dyes as active media in lasers has resulted in laser systems capable of being tuned over very wide spectral ranges. Dyes are used as passive mode lockers to produce short optical pulses and as Q-switching media to produce high power optical pulses.

One characteristic of all dyes used in lasers is the presence of broad bands in their energy levels. A representative energy level diagram is shown in Figure 2.1 [9]. The levels are divided into the two categories of singlet and triplet states according to the electronic spin. Within each spin state, there are electronic energy levels which are broadened by the vibrational and rotational states of the molecule. The electronic levels are separated by $10^4 cm^{-1}$, and the separations of the rotational and vibrational states are 1000 cm^{-1} and 1-10 cm^{-1}. The great size and complexity of organic dye molecules results in a near degeneracy of many vibrational and rotational energy levels. The practical significance of this great density of states is a nearly uninterrupted band of absorption and fluorescence. Thus, dye lasers can be pumped with a wide variety of optical sources, and can be tuned to provide output over a broad spectrum.

The ideal operation of a dye laser involves the optical excitation

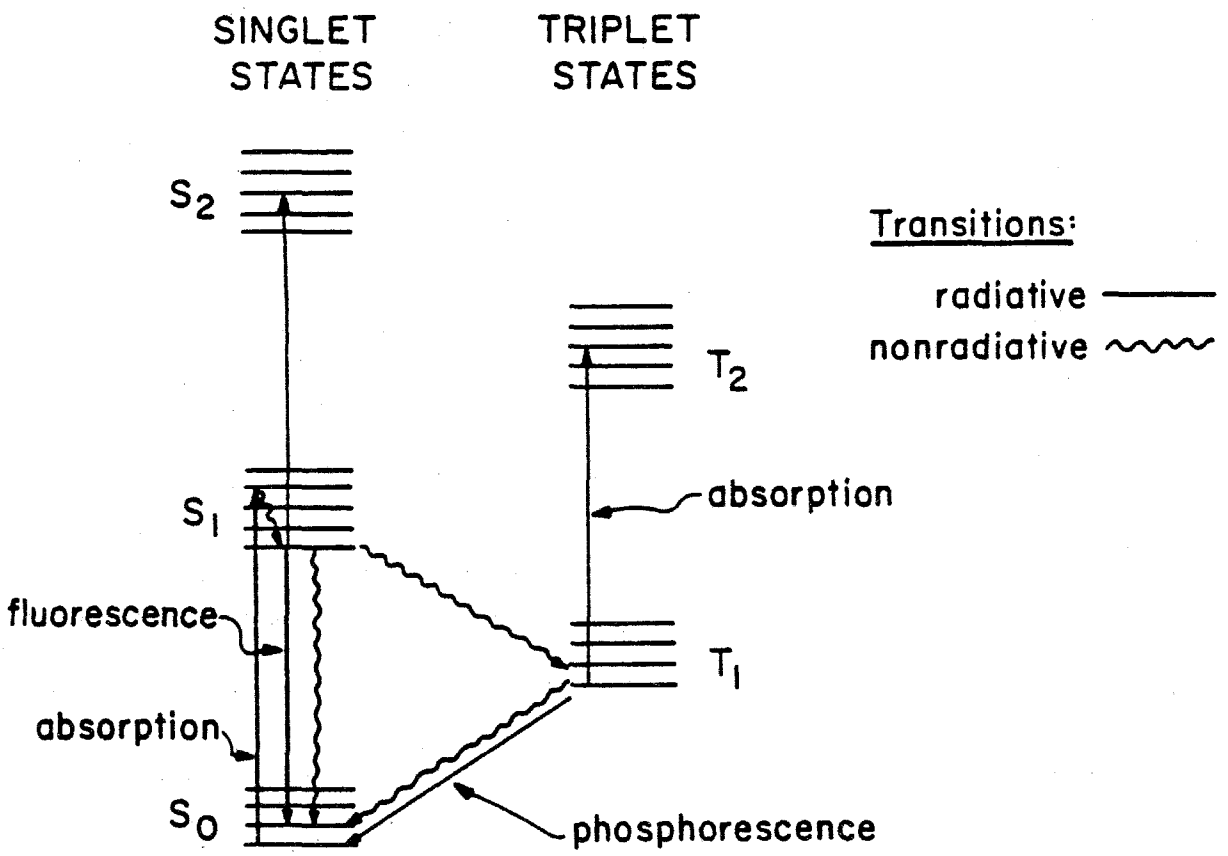

Figure 2.1 A schematic energy level diagram of a dye molecule

of an electron from the lowest electronic level of the singlet set of states to the first excited level. The relaxation of this electron to the bottom of the first excited level takes place nonradiatively within a few picoseconds. Stimulated emission of a photon by the excited electron drops the electron down to the lowest level again.

Problems encountered in the operation of dye lasers include the population of the triplet spin states. This occurs as a nonradiative transfer of excited electrons from the first excited singlet state to the bottom triplet state. If this triplet state becomes occupied, the probability of pump absorption from T_1 to T_2 is correspondingly enhanced. Further, the lowest triplet state can be long lived (on the order of milliseconds), meaning that the T_1 state would be a highly probable state for electrons after optical excitation. Thus, as a result of triplet state population, not only does the singlet inversion become depleted, but the pump power is wasted into an unwanted emission band.

Organic dyes exhibit fairly uniform spectral characteristics. Both the absorption and emission curves are broad, typically spanning 1000 wavenumbers. The emission peak is at a longer wavelength than the absorption peak; this is due to the fast relaxation of electrons to the lowest lying vibrational states. The fluorescence lifetimes of laser dyes are generally on the order of nanoseconds, but these lifetimes can be as short as tens of pi-

coseconds. Such short-lived dyes can find application as fast saturable absorbers.

2.2 Mode Locking a Dye Laser With a Saturable Absorber

There have been a number of theoretical analyses of the passively mode locked laser [7,8,12]. These discussions consider the simultaneous effects of a saturable absorber and a saturable amplifier in a laser cavity. The results these analyses obtain establish the optimum conditions for the production of ultrashort pulses from a passively mode locked laser.

There are two important conditions for this optimization that affect the design of the laser[8]. One requirement is that the spontaneous emission lifetime of the amplifier be comparable to the round trip time of the laser cavity. This ensures that the amplifier is recovered sufficiently to amplify the pulse upon its return. Further, the absorption cross section of the saturable absorber must be more than twice the amplification cross section of the gain medium. This will result in the saturation of the absorber at an earlier time (in the local time frame of the pulse) than the saturation of the amplifier. Thus, the absorber is bleached before the arrival of the pulse maximum (trimming the leading edge) and the amplifier is exhausted after the pulse maximum, reducing the gain of the trailing edge. In our laser, the ratio of the cross sections is

approximately 4:1.

Haus developed an analytic model which describes the passively mode locked system in terms of the material and operating parameters. The result he obtained was determined in terms of the spectral bandwidths, saturation energies, the interaction cross-sections, and the relaxation lifetimes of the two dyes. Haus found that the steady-state pulse intensity profile was a squared hyperbolic secant,

$$I(t) \propto sech^2(t/t_p) \qquad 2.1$$

Where t_p is proportional to the pulse width. This result is of importance in the determination of the specific pulse width from data acquired in autocorrelation experiments. This technique will be discussed later.

2.3 The Gain Medium of the Mode Locked Dye Laser

The organic dye with the highest known lasing efficiency is Rhodamine 6G. For this reason, it was used in the first CW dye laser, and was used as the gain medium for the mode locked dye laser. Its quantum efficiency is 83% [10], its absorption band ranges from the ultraviolet to 5500angstroms, and its lasing band ranges from 5700 angstroms to 6400 angstroms. The fluorescence lifetime for Rhodamine 6G is about 5 nanoseconds [11], so the round trip time of the

cavity was chosen to be 11 nanoseconds in order to allow the amplifying inversion sufficient time for recovery between pulses [12].

The dye laser is operated continuously, pumped with five watts of continuous optical power from an argon laser. In order to prevent the dye from boiling, and in order to minimize the population growth of the triplet state, the dye is passed through the cavity in the form of a jet. The spot size of the laser at the jet is approximately 30μm, and the speed of the jet is 10-12 m/sec. Thus, the dye is constantly being replenished, and whatever triplet state population is developed is physically removed from the laser in three microseconds.

2.4 The Saturable Absorbers in a Mode Locked Dye Laser

The dye laser is mode locked with a combination of two saturable absorbers, DODCI (3,3'-diethyl oxadicarbocyanine iodide) and malachite green. DODCI is a "slow" saturable absorber; bleaching effects of low power illumination disappear after approximately 1.2 nanoseconds [13]. Under high power pulsed illumination, such as within the mode locked laser cavity, its absorption recovery rate is stimulated to as fast as a few tens of picoseconds [14]. Malachite green is a fast saturable absorber with a relaxation time of two picoseconds [15].

When the mode locked dye laser was first developed, DODCI was

used alone as the saturable absorber. For the best results, it was necessary to operate the laser very close to threshold. Since the seven-mirror cavity is unusually complex, with the further destabilizing effect of two dye jets, it proved quite impractical to operate at a point where mechanical vibrations could terminate lasing altogether. It was later found that the addition of malachite green permitted successful operation of the laser sufficiently above threshold to ensure long range output stability [3].

Figure 2.2 shows a spectrophotometric trace of the saturable absorber solution. The optimum concentrations of the dyes are 36 micromolar for DODCI and 27 micromolar for malachite green. The saturation intensity for DODCI is $1.2x10^{6}W/cm^{2}$ which corresponds to a saturation energy (in a $7.5x10^{-7}cm^{2}$ spot size) of 1.2 nanojoules. Malachite green has a saturation intensity of 5.1×10^{8} W/cm^{2} and a saturation energy of 0.85 nanojoules. These energies are comparable to the picosecond pulse energy which is on the order of a nanojoule.

2.5 The Mode Locked Dye Laser Cavity Configuration

A diagram of the mode locked dye laser is shown in Figure 2.3. It features a seven mirror cavity with three waists. Two of the waists coincide with the location of the dye jets; the gain jet is Rhodamine 6G in ethylene glycol, and the saturable absorber jet is a

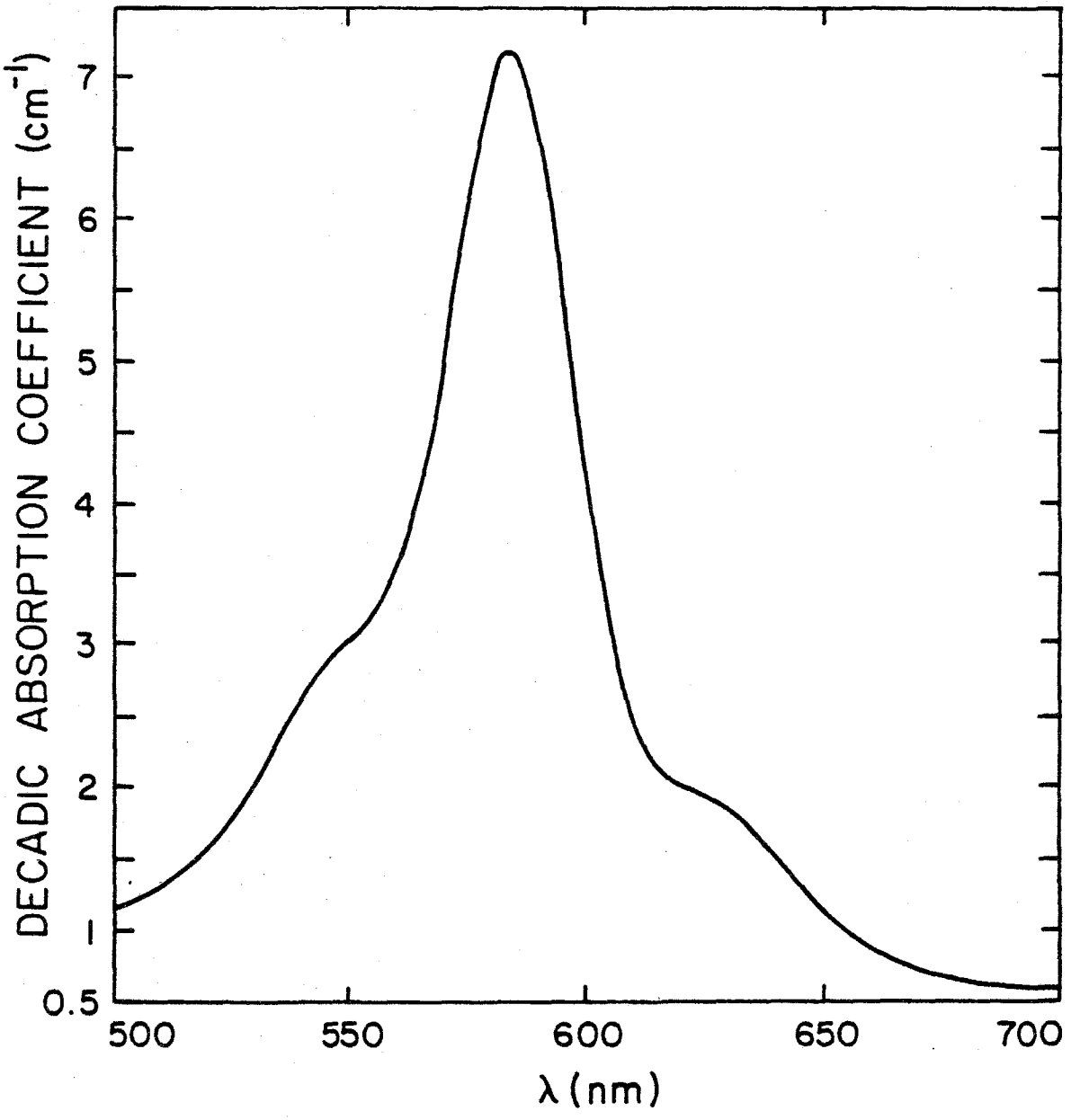

Figure 2.2 Absorption spectrum of a typical mixture of DODCI and malachite green, used to mode lock the dye laser.

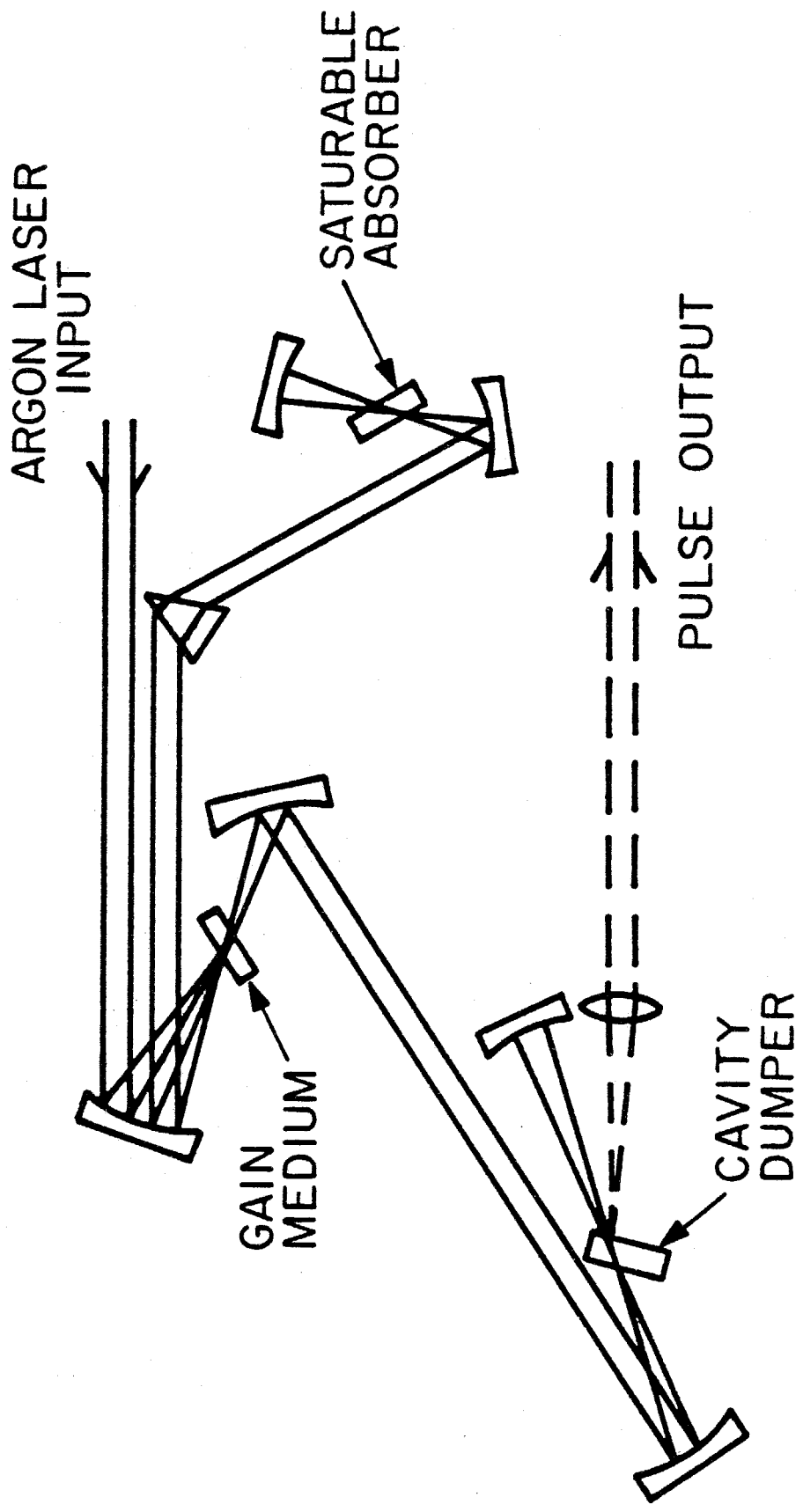

Figure 2.3 A schematic diagram of the passively mode locked CW dye laser with a dumper

mixture of DODCI and malachite green in ethylene glycol. The third waist is occupied by an acousto-optic Bragg cell for single pulse extraction from the cavity.

The argon laser pumping beam is focused to a 50 micron spot on the Rhodamine 6G dye jet. The cavity waist at that point is 42 microns in diameter, which results in efficient energy conversion. The absorber spot size is 27 microns in diameter in order to be more easily saturated by the picosecond pulse than the gain medium. The dumper spot size is 30 microns in order to establish fast acousto-optic pulse extraction.

The mirrors are coated for broad-band high reflectivity for the range 5500angstroms to 6500angstroms, and the pump focusing mirror is coated for 5145 angstroms as well. The cavity mirrors' placements and radii of curvature are chosen to optimize the stability of the cavity [16]. The mirrors are held in high-resolution angular orientation mounts, and one of the mounts at each cavity waist is placed on a translation stage for fine adjustments of the cavity length.

Each dye circulation system consists of a pump which draws dye from a reservoir and forces it through a 0.8μm filter. The dye is passed through a vibration damper and up to a stainless steel nozzle. The dye is forced through the nozzle, which has rectangular aperture dimensions of 1.58 x 0.39 mm. The resulting jet is flat and

optically clear, and relatively vibration free. The nozzle is held in a x-y-z translation stage as well as in an angular rotation mount which orients the plane of the jet at the Brewster angle with respect to the dye laser beam [17]

A prism is placed in the cavity to ensure that the laser oscillates at a wavelength within the effective mode locking range of the saturable absorbers. This range is 5900 to 6150 angstroms. The prism is cut at a full Littrow angle of 69° so that the dye laser is incident upon the prism at the Brewster angle at both faces.

If the output of the laser were obtained with a partially transmitting mirror, optimum output coupling considerations would dictate that the transmission be quite low, approximately two or three percent. In our system, the output coupling is performed with an acousto-optic cavity dumper with a maximum diffraction efficiency of 47%. As a result, we obtain at least ten times the output power that is obtained with conventional mirror coupling techniques.

The cavity dumper, or Bragg cell, consists of a block of fused silica oriented at the Brewster angle. An acoustic transducer is bonded to the bottom face of the block; when the transducer is energized by an rf electrical pulse, the resulting periodic strain wave acts as a transient grating. The cell is oriented at the Bragg angle

as well, and the laser beam is deflected out of the cavity for as long as the grating remains in the path of the beam [5b].

The cavity dumper used in the laser is a commercial argon laser acousto-optic dumper obtained from Spectra-Physics (Model 365). It is energized with an rf wave at 470 Mhz. This rf power comes from the Spectra-Physics driver, which is capable of emitting twelve watts of rf power with a rise time of five nanoseconds. The risetime of the laser output envelope is a convolution of the acoustic wave risetime and the transit time of the acoustic wave across the laser beam. The Bragg cell is placed at the third waist in the cavity, which has a beam diameter of $30\mu m$. Since the velocity of sound in the fused silica cell is $5.95x\,10^5$ cm/sec, the transit time of the wave is five nanoseconds. Thus, the overall risetime is sufficient to bring the acoustic wave to full power in the path of the laser beam within one cavity round trip time. Hence, a single pulse may be extracted from the cavity with minimal dumping of the preceding and succeeding pulses.

The dumper has a diffraction efficiency η given by

$$\eta=\sin^2\left|\frac{\pi L\sqrt{MI_a}}{\lambda\sqrt{2}}\right| \qquad 2.2$$

where L is the interaction length, M is the acousto-optic figure of merit, and I_a is the acoustic intensity. Using the peak acoustic

power available from the transducer, $16MW/cm^2$, and a figure of merit of $1.51x10^{-15}$ [18], the maximum η becomes 98%; in practice, only a 47% diffraction efficiency is obtained into a single diffraction order. The Bragg cell actually dumps two output beams from the cavity (see Figure 2.4). One of the beams passes once through the cell; it is Doppler up-shifted according to the configuration shown. Its power is ηP, where P is the intracavity power. The other beam is Doppler down-shifted, and passes through the cell twice. This beam consists of that cavity energy that is undiffracted upon the first pass and diffracted upon the second pass. Its power is $\eta(1-\eta)P$, which is always less than the power of the first beam.

The action of the dumper perturbs the mode locked laser away from its steady state condition of optimum pulse width and power. In order to extract the highest quality picosecond pulses from the laser, the gain medium must be given time to amplify the intracavity energy back to its original level. The saturation effects must be given an opportunity to restore the short pulse width of the pulses as well. According to Yasa [19], the minimum time required for complete restoration of the attributes of the pulses is 200 round trips. We allow our system 2048 round trips of recovery in case the stability of the laser falls short of the theoretical model used by Yasa.

It is necessary to synchronize the cavity dumper with the single

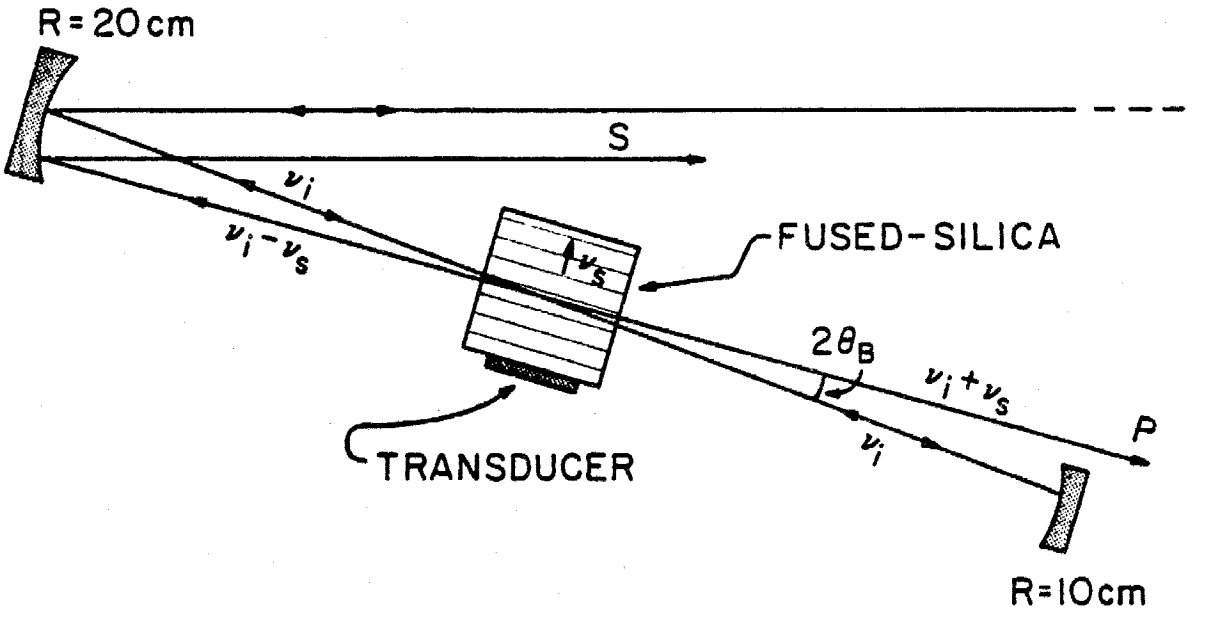

Figure 2.4 The dumper arm. P is the primary beam extracted from the cavity, S is the secondary one (see text).

pulse traveling within the laser(See Figure 2.5). This is done by directing some of the spurious reflections from the prism to a fast (200 picosecond risetime) photodetector[20]. The amplified output of this photodetector acts as a clock for the rest of the electronics in the system. The electrical pulse train is fed into a tuned amplifier resonant with the cavity round trip frequency, and counted down by 2048 [26]. This produces a pulse every 22μsec.. This pulse activates the rf driver for the cavity dumper, which produces a burst of 470 Mhz power to the acoustic transducer. The acoustic wave is now synchronized with the picosecond pulse in the cavity. The simplest way to adjust the relative delay between the light pulse and the acoustic wave is to move the transducer toward or away from the beam while monitoring the dumped output light pulse. The delay is increased when the sound wave has farther to travel, and as long as the total distance from the transducer to the laser beam is kept small, the acoustic wave maintains a clean wavefront. Proper adjustment gives the result shown in Figure 2.6. This oscilloscope trace is the output of the fast (200 psec) photodiode and is distinctly detector limited in its temporal response.

2.6 The Operation and Control of the Dye Laser

The mode locked dye laser is composed of an unusually complex cavity. The cavity consists of seven mirrors and four optical elements, all of which must be within microns of their optimum po-

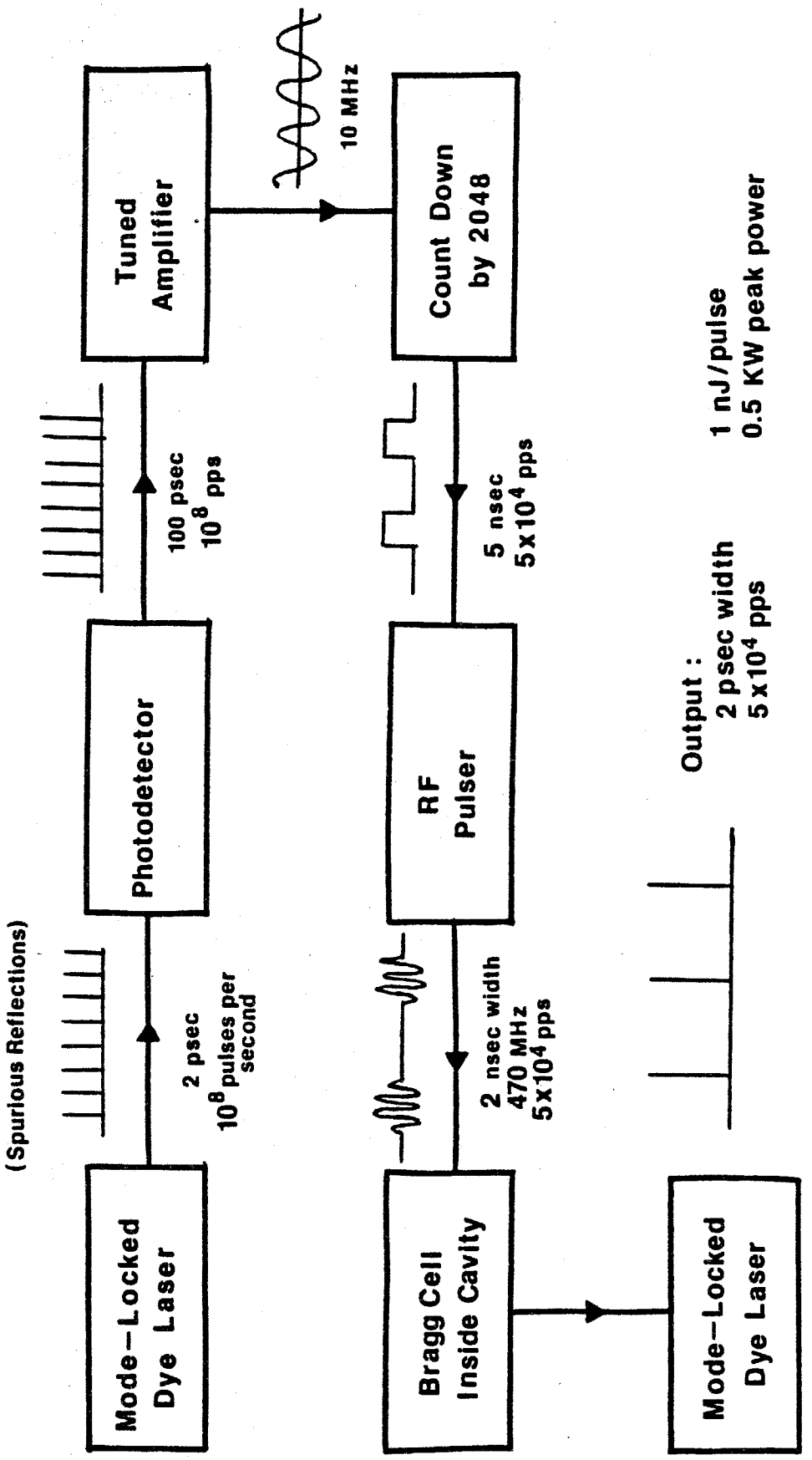

Figure 2.5 PULSE EXTRACTION TIMING SYSTEM

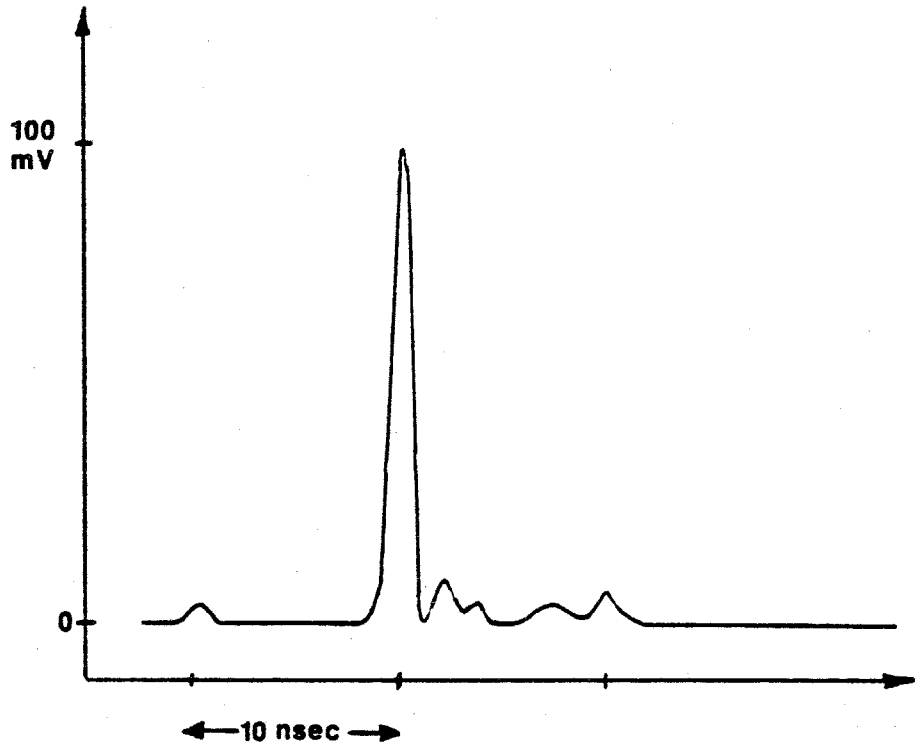

Figure 2.6 A detector limited display of a dumped picosecond pulse. Note remnants of the previous and following pulses at ±10 nsec from the main pulse.

sition for successful production of picosecond pulses. Each of the seven mirrors has two angular and two positional degrees of freedom. The two dye jets must be precisely centered on the appropriate cavity waist and oriented at the Brewster angle. The acousto-optic dumper must be oriented at the Brewster angle and the Bragg angle, and have its transducer placed precisely at the cavity waist of the dumper arm. Thus, it is necessary to establish a dependable means of converging on the small "volume" in a 37-dimensional space of cavity element co-ordinates that could produce a stable train of short pulses. Further, once the laser oscillates, it is important to be able to interpret the behavior of the laser to remedy departures from perfect alignment.

The first steps toward alignment of the laser involve a four mirror cavity which includes the tuning prism. Here, the DODCI and dumper cavity arms are replaced with flat mirrors at the location of beam waists of the seven mirror cavity. The four mirrors are placed in the approximate positions specified by a complete cavity stability analysis [16]. The concave mirrors placed about the Rhodamine 6G jet collimate the fluorescence, and direct it toward the flat mirrors. Lasing is directly forthcoming, and through cavity adjustment, the threshold is lowered to a few hundred milliwatts of argon power. The remaining two arms and the Bragg cell are introduced into the cavity; with each addition to the cavity,

there is an increase in threshold and a decrease in the tolerance of the cavity to misalignment. When the seven mirror cavity is complete, the threshold is 700 mW of argon power and the angular mirror tolerance is tens of microradians. Since the saturable absorber is only effective within a range of 6000 angstroms to 6150angstroms, the laser is tuned with the prism to oscillate in that spectral region.

The saturable absorber jet is first introduced into the cavity with no dyes in solution. As the dyes are introduced, the laser intensity begins to oscillate at the round trip frequency. As the dye concentrations are increased to their optimum level, the lasing pump threshold reaches roughly five watts, and the intensity modulation sharpens to form pulses. The optimum dye concentrations are determined empirically, and correspond to the absorption curve shown in Figure 2.2. The pulses become detector limited; a typical display is shown in Figure 2.7. We use two means of obtaining more precise knowledge of the laser operation. The most direct method is second harmonic generation pulse measurement, but a more convenient technique that has proven to be a very reliable indicator of the pulse quality is the real-time spectral measurement using the optical multichannel analyzer.

When the the power of the argon pump laser is raised just beyond the threshold of the dye laser, the dye laser spectrum shows a broad, stable profile (see Figure 2.8). This is indicative of

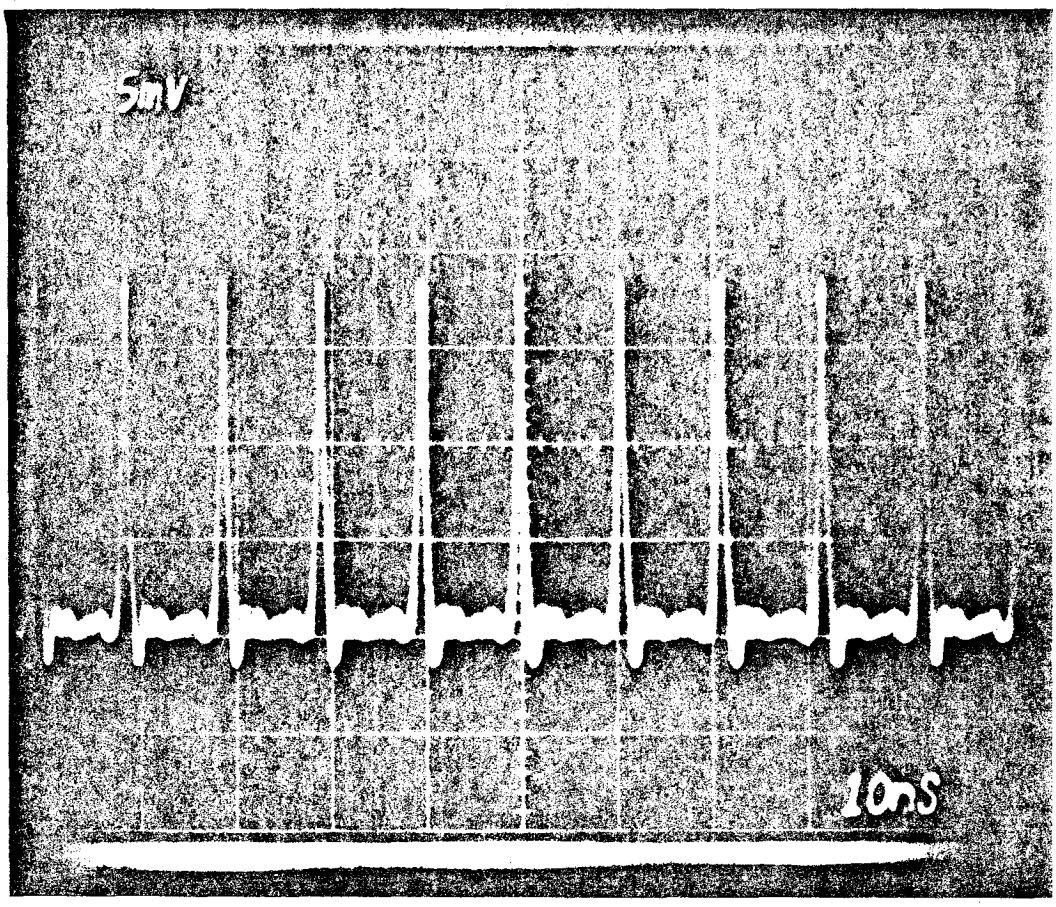

Figure 2.7 Detector-limited pulses generated by the passively mode locked CW dye laser.

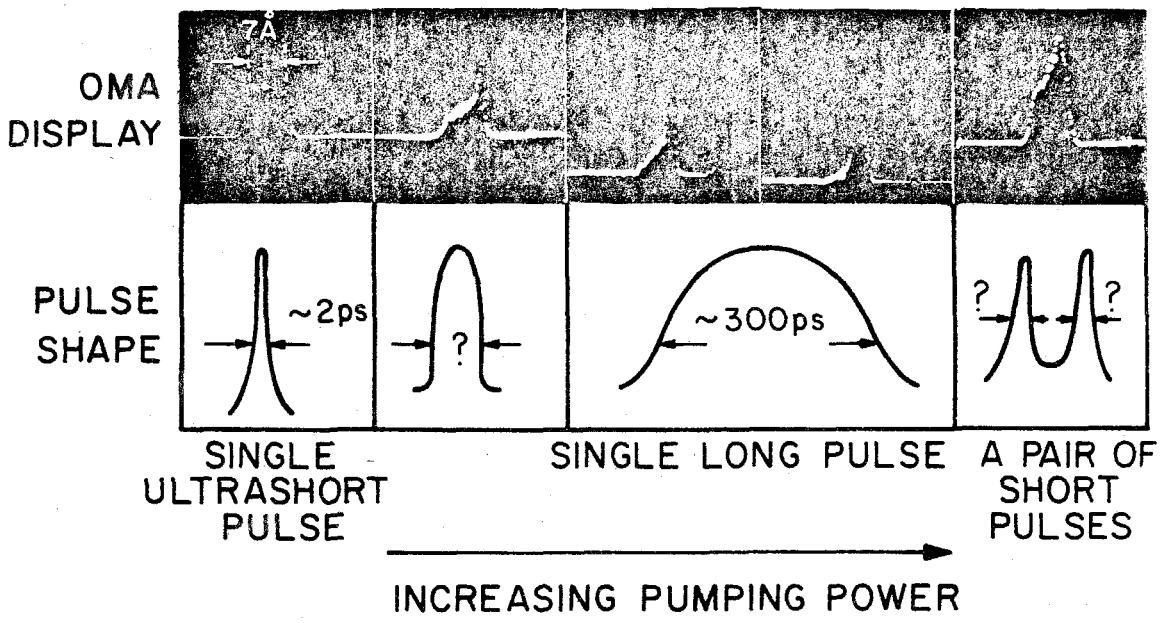

Figure 2.8 Some typical laser pulse shapes and the related spectra at various pump levels.

short output pulses. If the argon power is raised further, or if the concentration of the saturable absorber is too low, the spectrum narrows, and shows a spike in a spectral region where the saturable absorber is being excessively bleached. When this happens, the absorber is incapable of adequately attenuating the leading edge of the pulses, the inversion in the amplifier is incompletely depleted, and the pulses broaden to a few hundred picoseconds. If the pumping power is raised still further, the laser begins double pulsing. Here, the gain is sufficient to support two fairly short pulses, each capable of saturating the absorber. The spectrum broadens somewhat as well. With continued increase of the pumping power, the pulses disappear entirely, and are replaced with the modulation observed with small absorber concentrations. At this and higher power levels, the spectrum narrows to no more than a few angstroms. Finally, all modulation disappears if the dye laser is given sufficient gain to saturate the absorber on a CW basis. While there is some tradeoff between pumping power and absorber concentration, the shortest pulses are only obtained with the proper saturable absorber concentration designated in Figure 2.2.

2.7 Summary of the Operation Characteristics

The operating parameters of the passively mode locked dye laser can be summarized as follows: The argon laser is stabilized for constant light output, and emits five watts of continuous power

at 5145 angstroms. The dye laser generates pulses of 1-2 picosecond duration, with peak powers of about 1 kW. This corresponds to about 1 nanojoule of energy per pulse, or 10^8 photons per pulse. A pulse is dumped from the laser every 2048 round trips of the cavity, or every 22 microseconds.

Chapter 3

Picosecond Pulse Width Measurements

3.0 Introduction

Figure 2.6 in the previous chapter showed the output of the mode locked dye laser using a fast photodetector. This detector was far too slow to resolve the pulse shape. While significantly faster photodetectors have been developed and are commercially available, the fastest real time electronic means of measuring the picosecond pulses is no faster than ten to twenty-five picoseconds. The fastest measurement techniques involve sampling oscilloscopes or streak cameras for the final signal display, and to this date, no such devices have shown sufficiently fast response to resolve a sub-picosecond pulse.

The fastest direct pulse measurement system is the streak camera. Recent improvements in the response time of these devices has resulted in a temporal response of a few picoseconds[21]. The drawback of streak cameras is their high cost and their single-shot nature. If multiple shot averaging is desired, a signal averaging system, such as an optical multichannel analyzer, is necessary.

Less costly methods of pulse measurement include two-photon fluorescence (TPF) and second harmonic generation (SHG) [22,23].

TPF requires a fluorescent dye to absorb light in a two photon process from two counterpropagating beams. Where the pulses coincide in space, there will be maximum TPF, and the profile of the pulse's autocorrelation is obtained. A similar principle is invoked in SHG, where the only resulting information regarding the temporal shape of the pulse is the autocorrelation integral. As will be seen, this gives the actual pulse width to an accuracy of within a factor of two. In our situation, the TPF technique would suffer due to low signal strength; the SHG method provides easily detectable signals, and is generally regarded as a superior means of dye laser pulse measurement.

3.1 The Second Harmonic Generation Technique of Pulse Width Measurement

SHG picosecond pulse width measurements involve splitting the pulses in two with a beamsplitter (See Figure 3.1). Each beam is sent down a separate arm of a Michelson interferometer, where each pulse experiences a delay τ proportional to the length of the particular arm. The two pulses
are focused on, and coincide in a crystal of KDP (potassium dihydrogen phosphate), a second harmonic generating medium. Since SHG is a nonlinear phenomenon, there is disproportionately more average second harmonic energy produced when the pulses arrive at the crystal simultaneously than when they arrive separately.

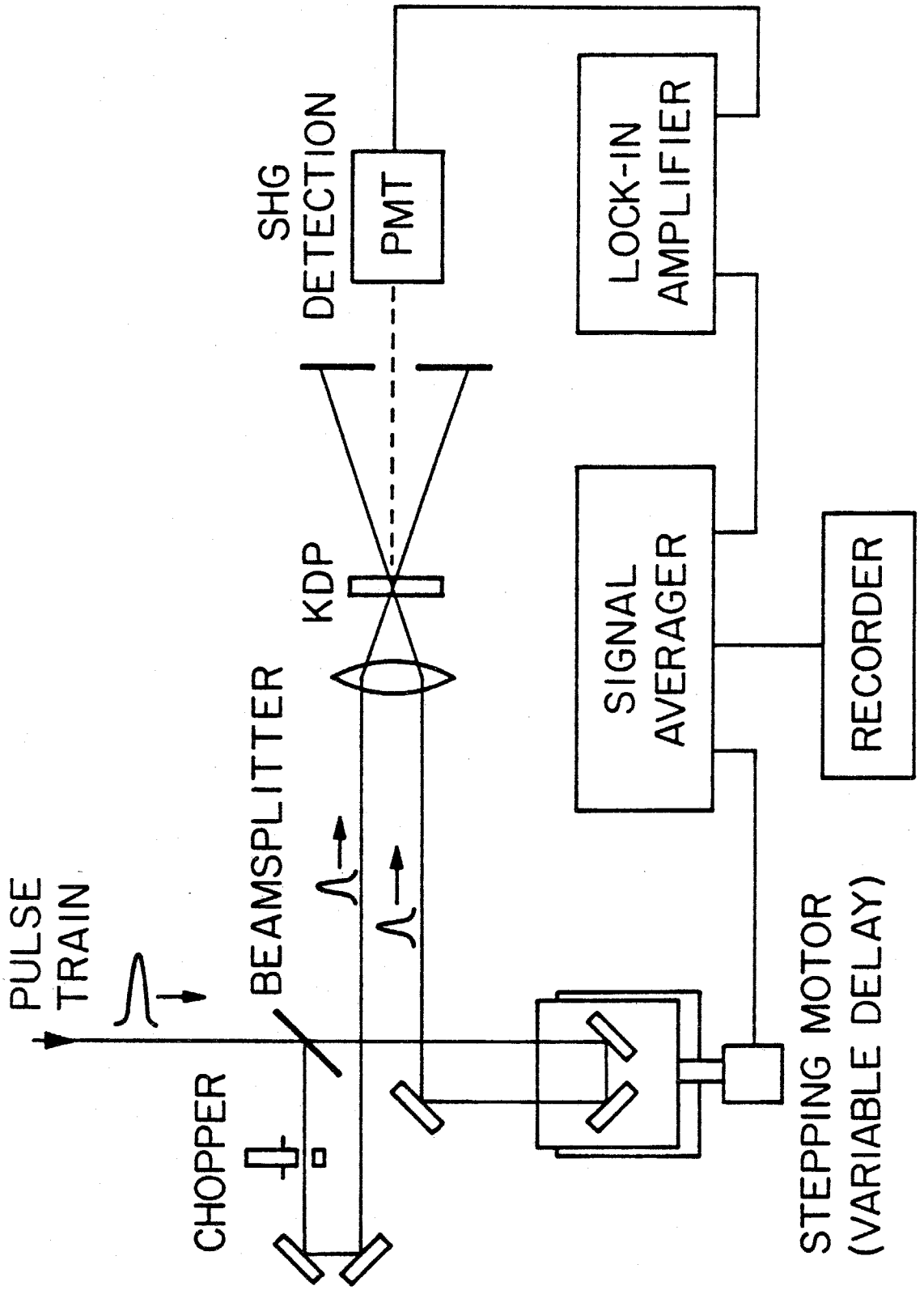

Figure 3.1 Second harmonic generation set up for pulse autocorrelation measurements.

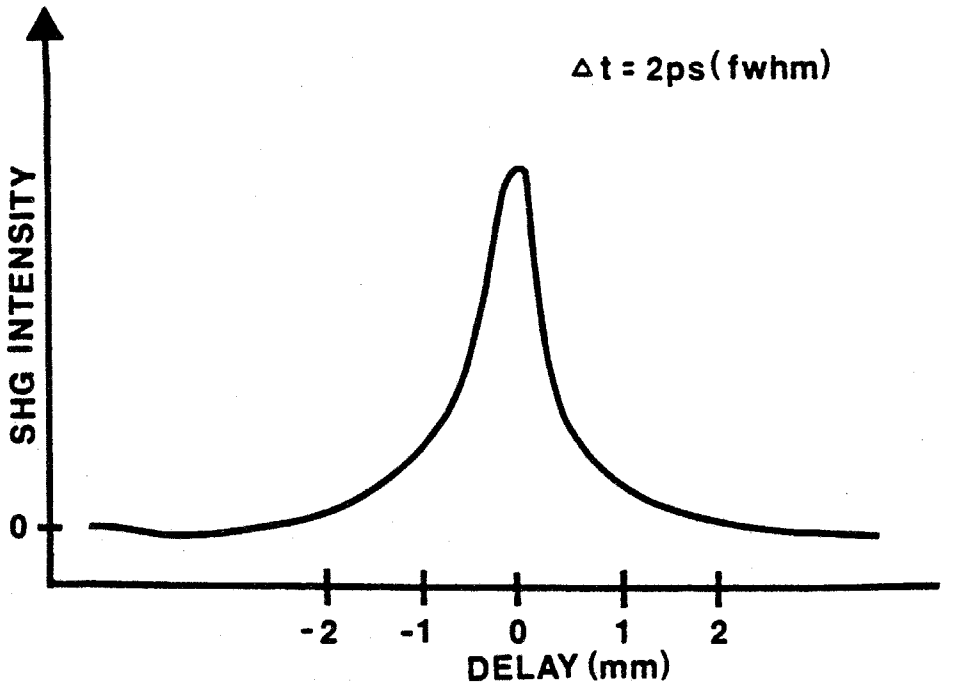

Figure 3.2 A typical trace of a noncollinear second harmonic generation pulse width measurement.

Thus, by measuring the average SHG as a function of optical delay, one can deduce the spatial (i.e., temporal) extent of the picosecond pulse. The spatial extent of a 1 picosecond pulse in space is 0.3 mm.

If an optical wave is incident upon a crystal with a nonlinear susceptibility, there will be a polarization induced with a component oscillating at double the frequency of the incoming wave. This polarization drives a second harmonic optical field, and if proper phase matching is established, the superposition of all these driven fields is a coherent frequency-doubled beam[5c]. Specifically, a wave polarized in the β direction

$$E(t)=\tfrac{1}{2}[E_{\beta}^{\omega}e^{i\omega t}+c.c.] \qquad 3.1$$

generates a polarization oscillating at 2ω in the α direction

$$P_{\alpha}^{2\omega}=\frac{d_{\alpha\beta\beta}}{4}[E_{\beta}^{\omega}e^{i\omega t}+c.c.]^2 \qquad 3.2$$

where $d_{\alpha\beta\beta}$ is the nonlinear susceptibility.

In the case of picosecond pulse width measurements, the electric field amplitude E_{β}^{ω} is the pulse envelope, and thus varies with time.

$$E_{pulse}(t)=\tfrac{1}{2}[E_{\beta}^{\omega}(t)+c.c.] \qquad 3.3$$

If two pulses are delayed in time by a relative amount τ, and superimposed at the SHG crystal, the resulting nonlinear polarization is

$$P_\alpha(t)=d_{\alpha\beta\beta}E^2_{total}=\frac{d_{\alpha\beta\beta}}{4}[E_\beta(t)e^{i(\omega t+\vec{k}\cdot\vec{r})}+E_\beta(t+\tau)e^{i(\omega(t+\tau)+\vec{k}\cdot\vec{r})}+c.c.]^2 \qquad 3.4$$

The component of this polarization oscillating at 2ω is

$$P^{2\omega}_\alpha(t)=\frac{d_{\alpha\beta\beta}}{4}[E^2e^{2i(\omega t+\vec{k}\cdot\vec{r})}+E^2_\tau e^{2i(\omega(t+\tau)+\vec{k}\cdot\vec{r})}$$
$$+2EE_\tau e^{2i(\omega t+\vec{k}\cdot\vec{r})}e^{i\omega\tau}+c.c.] \qquad 3.5$$

where E is $E^\omega_\beta(t)$ and E_τ is $E^\omega_\beta(t+\tau)$.

This polarization drives a SHG electric field. The derivation of this field from the inhomogeneous wave equation yields the expression [5]

$$E_{SHG}\ \alpha\ d_{\alpha\beta\beta}E^2_{total}\frac{e^{i\Delta kL}-1}{i\Delta k} \qquad 3.6$$

where $\Delta k=k_{2\omega}-2k_\omega$ represents a mismatch in the phase velocities of the fundamental and SHG waves, L is the interaction length of the process, and E_{total} is the superposition field of the two pulses.

The SHG power is proportional to the squared amplitude of the SHG electric field

$$Power_{SHG}\ \alpha\ E_{SHG}E^*_{SHG} \qquad 3.7$$

For the moment, let us assume perfect phase matching: $\Delta k=0$. Combining Equations 3.6 and 3.7, and keeping only the slowly varying terms (compared to optical frequencies), we obtain

$$Power_{SHG} \propto I^2+I_\tau^2+4II_\tau \quad +(E^2E_\tau^{2*}\, e^{-2i\omega\tau}+2(I+I_\tau)EE_\tau^*\, e^{-i\omega\tau}+c.c.) \qquad 3.8$$

where the intensity $I\equiv EE^*$, and $I_\tau\equiv E_\tau E_\tau^*$.

The process of SHG pulse width measurement consists of sweeping τ roughly linearly through an interval centered at $\tau=0$. A photomultiplier detects the SHG, and its output is integrated with a low-pass filter to obtain an electric current representing the average contribution of many pulses. The rate f at which $\tau=ft$ is swept is such that ωf exceeds the cutoff frequency of the filter. Hence, the terms in Equation 3.8 which oscillate at $\omega\tau$ and $2\omega\tau$ average to zero, leaving only the first three terms. The cutoff frequency of the filter is also well below the repetition rate of the picosecond pulses, so the SHG current may be accurately represented by the integral of the slowly varying terms in Equation 3.8 over some interval containing many picosecond pulses.

$$i(\tau)=\int\{I^2(t)+I^2(t+\tau)+4I(t)I(t+\tau)\}dt \qquad 3.9$$

Integrating and normalizing so that $\lim_{\tau\to\infty} i(\tau)=1$, Equation 3.9 becomes

$$i(\tau)=1+2G^{(2)}(\tau) \qquad 3.10$$

where G is the autocorrelation integral, given by

$$G^{(2)}(\tau)=\frac{\int I(t)I(t+\tau)dt}{\int I^2(t)dt} \qquad 3.11$$

The range of G is 0 for $\tau\to\infty$ and 1 for $\tau=0$, so the ratio of the peak value of i(t) to the minimum baseline is 3:1.

Thus, the SHG data will give information about the pulse, but only through the autocorrelation integral of the pulse. In practice, the shape of the pulse is assumed, and the analytic autocorrelation integral is compared to the experimental SHG curve. In chapter two, it was stated that the theoretical prediction of I(t) was a squared hyperbolic secant. If the autocorrelation integral is performed on the theoretical function, the ratio between the FWHMs of the integral and the function is 1.55. In the same manner, the ratio of the width of the experimental SHG curve and the actual pulse width would be 1.55. Regardless of the choice of the function used to describe the pulse width, the ratio of FWHMs is on the order of unity, and for rough measurements, the difference between the two widths is ignored.

One of the arms of our Michelson interferometer is movable by means of a precision stepping motor and translation stage, and the other arm has a rapidly oscillating (60 Hz) optical delay apparatus. These features of the interferometer allow either a slow and accu-

rate variable delay to be introduced between the two pulses, or a fast, approximate delay suitable for real time observation of the pulse width. The rapid delay apparatus has an analog output signal roughly proportional to the delay. This signal is used to drive the horizontal axis of an oscilloscope, and the SHG signal drives the vertical axis. The display is a real time pulse measurement, which is a valuable monitor of the pulsewidth for use in cavity alignment and pumping power optimization. The slow and accurate SHG measurement data are loaded into a Nicolet 1174 signal averager and are averaged over many traversals of the translation stage. This lowers the noise in the signal, and provides a numerical record of the autocorrelation data on magnetic tape for later analytical studies.

Figure 3.3 shows the general characteristics of SHG traces, and how the technique indicates the quality of mode locking that prevails in a laser. When the laser is unlocked, and the modes oscillate with random relative phases, the SHG shows a coherence spike at $\tau=0$. If the laser is completely locked, then the modes are coherently related to each other, and the coherence length increases to the extent of the pulse width. At intermediate stages of mode locking, the SHG is a superposition of the two extreme cases [24].

A significant reduction in the noise of the SHG analysis is pos-

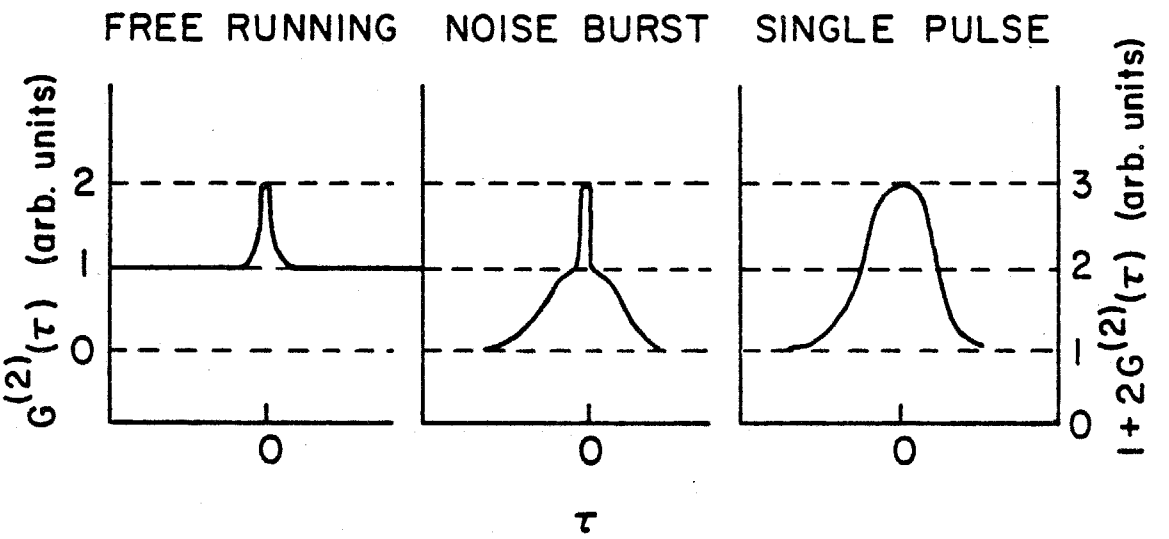

Figure 3.3 Autocorrelation traces for pulses with varying degrees of coherence. The left ordinate is for noncollinear SHG, and the right ordinate is for collinear SHG.

sible if the input beams are non-collinear. This results in the complete absence of phase matching when only one pulse is present in the nonlinear crystal. So, instead of a peak of three units on a baseline of one unit of SHG power, the non-collinear SHG peak is obtained on a zero baseline. Moreover, the fundamental beams are physically separated from the SHG beam at the detector, allowing spatial filtering to reject the noise. One drawback of the non-collinear approach is that the interferometer must be set for near-zero delay when aligning the KDP crystal, since one beam alone does not generate the SHG. Without SHG, it is difficult to know where the zero delay point is; consequently, a simutaneous search of delay and KDP orientation must be made to find the SHG. With the collinear method, the SHG baseline can be found first,then the delay is varied to find the maximum.

The limitations of the SHG pulse measurement technique include the fact that the autocorrelation integral of a pulse need in no way resemble the actual pulse. For example, the autocorrelation of a pulse is always symmetric about $\tau=0$, regardless of any asymmetry of the pulse. Further, the averaged SHG data is biased toward the detection of short pulses [25]. Due to the nonlinear nature of SHG, the broader pulses that may exist in a pulse train make less of a contribution to the average SHG power than the sharper pulses. For example, the dye laser frequently develops

spontaneous pulse height modulation at a 200 kHz frequency. In all likelihood, the pulse width is being modulated as well. With some effort in adjusting the cavity, this modulation can be suppressed. Such steps must be taken to establish a stably oscillating cavity in order to rely on the pulse width determined by SHG. Another difficulty with the autocorrelation measurement is the requirement of a clean, nearly Gaussian transverse mode in the output of the laser. Slight transverse misalignments of two fundamental modes will not greatly decrease the intensity product required for SHG. However, if high order modes suffer transverse displacement during the delay sweep, the intensity product could vary considerably, and completely destroy the accuracy of the SHG measurement.

This nonlinear method of correlating a fast pulse with another signal (including itself) through variable delay is a powerful technique suitable for application in a broad range of experiments. If the beam of picosecond pulses were split into a strong pump beam and a weak probe beam, the probe could be used to determine the lifetime of effects that the pump beam had on a sample. If the pump were sufficiently intense to bleach a fast saturable absorber, for example, the detection of the transmission of an obliquely introduced probe would demonstrate the persistence of the bleaching. If the probe pulse arrived at the absorber before the pump, it would be absorbed; if it arrived after the pump, the probe would

pass through the bleached absorber. By varying the delay between the two pulses, the bleaching lifetime could be measured with picosecond resolution. The same principles apply to reflection or polarization rotation studies in semiconductors and other materials.

3.2 The Experimental Set-up for Pulse Width Measurement

Our second harmonic generation system is shown in Figure 3.1. It is based upon the system first developed at Bell Laboratories by Ippen and Shank[3]. It consists of the interferometric delay system, a KDP crystal, and a detection and signal processing system.

The interferometer consists of the two delay arms mentioned earlier. The accurate arm has a resolution of 21 femtoseconds in optical delay, and a total range of 500 picoseconds. The oscillating arm has a resolution of about 0.5 picoseconds (limited by the speed of the detection system), and a range of 100 picoseconds.

In order to produce significant quantities of second harmonic output, it is necessary to match the phases of the fundamental beams and the second harmonic beam[5c]. This ensures a coherent superposition of all the second harmonic wavelets created throughout the crystal. This is possible in the KDP crystal, since it possesses birefringence. The input and output beams are of a

different polarization, so the refractive index of an ordinary ray at 6100 angstroms can be matched to an extraordinary ray at 3050 angstroms. If the input and output wavevectors are not matched, the second harmonic output over an interaction length L is reduced by a factor

$$\frac{\sin^2(\Delta kL)}{(\Delta kL)^2} \qquad 3.12$$

where $\Delta k = k_{2\omega} - k_{1,\omega} - k_{2,\omega}$, i.e., the difference between the SHG wavevectors and the two fundamental wavevectors. If Δk can be made equal to zero, the maximum SHG can be obtained.

$\Delta\vec{k}$ can be made equal to zero by specifying the orientation of the crystal relative to the input beams. The input beams are non-collinear; so the phase matching requirement is satisfied in the direction of the angle bisector of the two beams. If the input beams are separated by an angle 2β, then the phase matching condition becomes $k_{2\omega} = 2k_{\omega}\cos\beta$ or

$$n_e^{2\omega}(\vartheta) = n_o^{\omega}\cos\beta \qquad 3.13$$

where ϑ is the angle that the bisector makes with the optic axis of the crystal. $n_e^{2\omega}(\vartheta)$ is the extraordinary refractive index at 2ω at an angle ϑ to the optic axis, and n_o^{ω} is the ordinary refractive index at frequency ω. The angle ϑ is determined from an expression of the refractive index ellipsoid [5c]:

$$\sin^2\vartheta=\frac{(n_o^{\omega}\cos\beta)^{-2}-(n_o^{2\omega})^{-2}}{(n_e^{2\omega})^{-2}-(n_o^{2\omega})^{-2}} \qquad 3.14$$

In this case, λ=6100 angstroms, $n_e^{2\omega}$=1.496752, $n_o^{2\omega}$=1.543934, andn_o^{ω}=1.508818. The crystal was obtained from Cleveland Crystals, and was cut at ϑ=60° 28′ , so the half angle of the input separation is β=2° 5′

The phase mismatch has been set to zero through appropriate orientation of the crystal. However, the phase matching has only been established at the center wavelength of the pulse. In order to reduce the overall phase mismatch arising from the nonzero bandwidth of the pulse, the interaction length L must be short enough to make the product ΔkL small. The spread of $\Delta k=k_{e,2\omega}-2k_{o,\omega}\cos\beta$ at 6100 angstroms over a spectral range of 12 angstroms (a 1 psec pulse) is

$$\delta\Delta k=\frac{2\pi}{\lambda}(n_{e,2(\omega+\delta\omega)}(\vartheta)-n_{o,\omega+\delta\omega}) \qquad 3.15$$

Let $\zeta=n_{e,2\omega}(\vartheta)-2n_{o,\omega}$. For rough calculations, we assume $\partial\zeta/\partial\lambda$ is a constant. Thus,

$$\delta\Delta k=\frac{(\delta\lambda)\pi}{\lambda}\frac{\partial\zeta}{\partial\lambda} \qquad 3.16$$

Using established data for the wavelength dependence of the ordinary and extraordinary refractive index in KDP [5c], the maximum

interaction length L is

$$L_{max}=\frac{2\pi}{\delta\Delta k}=0.3cm. \qquad 3.17$$

Since the beams are non-collinear, and focused by a 5 cm. lens to a spot size of 15 microns, the actual interaction length is

$$L=\frac{spot\ diameter}{\sin\beta}=0.045cm. \qquad 3.18$$

Thus, the SHG can be expected to experience adequate phase matching over the entire interaction length.

The second harmonic beam is detected with an RCA 1P28 photomultiplier with a Schott UG-5 ultraviolet transmitting filter. The fundamental beam is rejected by the glass filter as well as by an aperture placed in front of the photocathode of the detector which allows only the normally incident second harmonic beam (see Figure 3.1). The integrated current from the photomultiplier is stored on a Nicolet 1174 signal averager. The signal averager contains 4096 addresses which can be loaded separately. Each address is associated with a given position of the translation stage (i.e., a given value of the delay time τ between the two incident pulses) through a master controller of the stepping motor and signal averager[26]. The stage is swept through the pulse width and the SHG signal is accumulated in the signal averager for processing

and interpretation.

Fourier transform considerations dictate that in order to produce short optical pulses, the lasing spectrum must be correspondingly broad. The spectral range is given by

$$\Delta\lambda = \frac{\lambda^2}{c\,\tau_{pulse}} \qquad 3.19$$

For 6100 angstrom pulses with a duration of 1 picosecond, the spectral bandwidth of the laser must be 12 angstroms. In order to monitor the real time spectrum of the dye laser, we couple spurious reflections from the Bragg cell into an optical fiber. The fiber carries the light to the entrance slit of a grating spectrometer (GCA Mcpherson 2051). The exit slit of the spectrometer is replaced with the vidicon of an optical multichannel analyzer (OMA). The vidicon (Princeton Applied Research 1205A)has 512 optical elements which are variously illuminated by the spectral components of the laser. These elements are connected to a set of addressable memories which are displayed on a CRT. This display indicates the real time spectrum of the dye laser. The spectral range of the system is 100 angstroms, and the resolution is 0.186 angstroms. The center wavelength of the display is determined by the orientation of the spectrometer grating; the calibration of the spectrometer-OMA system is checked with a He-Ne and an argon laser. The information yielded by the real-time spectral measurements gives valuable in-

sight into the operating conditions of the mode locked dye laser.

References for Part I

1. L. E. Hargrove, R. L. Fork, and M. A. Pollack, Appl. Phys. Lett. 5, 4 (1964).
2. C. V. Shank and E. P. Ippen, Appl. Phys. Lett. 24, 373 (1974).
3. E. P. Ippen and C. V. Shank, Appl. Phys. Lett. 27, 488 (1975).
4. E. P. Ippen and C. V. Shank in Topics in Applied Physics, ed. by S. L. Shapiro (Springer-Verlag, 1977), Ch. 4.
5. A. Yariv, Quantum Electronics (John Wiley and Sons, Inc., New York, 2nd ed, 1975), a) p. 256; b) p. 356; c) p. 421.
6. J. P. Laussade, Ph.D. Thesis, California Institute of Technology, 1969.
7. H. A. Haus, IEEE J. Quant. Electron. QE-11, 736 (1975).
8. C. P. Ausschnitt, IEEE J. Quant. Electron. QE-13, 321 (1977).
9. M. Bass, T. F. Deutsch, and M. J. Weber, Lasers, Vol. 3, Levine and DeMaria, eds. (Marcel Dekker, Inc., New York, 1971), Ch. 3.
10. B. B. Snavely, Proc. IEEE 57, 1374 (1964).
11. M. E. Mack, J. Appl. Phys. 39, 2483 (1968).
12. G.H.C. New, IEEE J. Quant. Electron. QE-10, 115 (1974).
13. C. V. Shank and E. P. Ippen, Appl. Phys. Lett. 26, 62 (1975).
14. G. E. Bush, R. P. Jones, and P. M. Rentzepis, Chem. Phys. Lett. 18, 178 (1973).
15. E. P. Ippen, private communication.
16. P. Agmon, Ph.D. Thesis, California Institute of Technology, 1980.
17. The mirrors were obtained from CVI Corp. or from Spectra Physics. The pump was obtained from the Weldon Tool Co. The vibration damper is the #A71530-200 from Greer Olaer Inc. The stainless steel nozzles are from Coherent, Inc. The x-y-z stages were obtained from the Line

Tool Co. The rotation mounts for the dye jets were designed and constructed by L. Begay.

18. R. W. Dixon, J. Appl. Phys. 38, 5149 (1967).

19. Z. A. Yasa, et al., Opt. Comm. 15, 354 (1975).

20. G. H. McCall, Rev. Sci. Instrum. 43, 865 (1972).

21. Hamamatsu Corporation.

22. H. P. Weber, J. Appl. Phys. 38, 2231 (1967).

23. J. A. Armstrong, Appl. Phys. Lett. 10, 16 (1967).

24. E. P. Ippen and C. V. Shank in Topics in Applied Physics, ed. by S. L. Shapiro (Springer-Verlag, 1977), Ch. 3.

25. E. W. Van Stryland, Opt. Commun. 31, 93 (1979).

26. The pulse extraction timing system was designed and constructed by Desmond Armstrong.

PART II. PICOSECOND PHOTOCONDUCTIVITY OF SEMI-INSULATING GALLIUM ARSENIDE

Chapter 4

The Opto-electronic Switch

4.0 Introduction

The introduction of deep impurity levels into gallium arsenide has been an effective means of producing semi-insulating samples of the material. Resistivities of $10^8 \Omega$-cm are typical for GaAs in which chromium or oxygen has been introduced. The great majority of our experiments have been performed on chromium doped material, but the general description of Cr:GaAs fits oxygen doped material as well. The addition of these dopants is designed to compensate for the presence of low level impurities such as silicon. Silicon contamination of GaAs is a common side-effect of growing the crystal in quartz (silicon dioxide) boats. The dopants also act as a recombination center for free electrons and holes, thus reducing the free carrier concentration by reducing the recombination lifetime. As a result, the concentration of electrons and holes in Cr:GaAs is typically as low as $10^6 cm^{-3}$, and the bulk recombination lifetime is well under a nanosecond.

It is due to these two properties of Cr:GaAs that this material

was chosen for photoconductivity studies. Our dye laser has 10^8 photons per pulse; for typical geometries of fast photoconductivity measurements, the highest possible photocarrier density would be $10^{14} cm^{-3}$. It was necessary to select a material for which the introduction of that concentration of photocarriers could be easily detected. Hence, the low free carrier concentration of Cr:GaAs was ideal; the ratio of dark to illuminated carrier densities (and corresponding currents) could be as much as eight orders of magnitude. In principle, then, such measurements could be taken with a high signal to noise ratio. Further, the subnanosecond recombination lifetime of the material was a feature that required the high temporal resolution of the mode locked dye laser. Thus, Cr:GaAs accommodated both the analytical strengths and weaknesses of the mode locked dye laser. Further, the use of Cr:GaAs in microwave devices and as a substrate material in opto-electronic devices motivated these studies in understanding ultrafast phenomena in the material.

High speed photoconductivity experiments have been performed on Cr:GaAs by a number of investigators [1-4]. The measurement technique generally consisted of mounting a chip of Cr:GaAs in the middle of a high-speed transmission line, applying a voltage to one end of the line, and observing the current pulse through the chip upon illumination by a fast optical pulse. The

risetime of these current pulses is typically as fast as the optical pulse risetime, or as fast as the line will permit. The falltime is dictated by the lifetime of the photocarriers, and the height of the current pulse is determined by the intensity of the photoexcitation. The efforts of these investigators have generally been directed toward the production of the fastest possible current pulses, or the highest possible output voltages. Since the devices "switch" the input voltage on or off the output terminals, they are commonly known as opto-electronic switches. The fastest switches have shown a 70 picosecond full-width at half maximum (FWHM) [1], and high voltage devices have switched several kilovolts [4].

The fast response time of these devices was generally attributed by the observers to the presence of chromium in the material. However, the presence of chromium alone as a recombination center cannot account for the high speed of the Cr:GaAs devices. A more accurate depiction of the dynamics of the switches must include the effect of surface recombination. Since the excitation pulses are completely absorbed within the first micron of the material, it is clear that surface effects could play a profound role in determining the effective lifetime of free carriers.

Our experiments have demonstrated fast photoconductivity of these switches; the fastest response time (FWHM) of the switches to picosecond pulses has been 70 psec. We have also seen that the

response of the switches depends upon surface effects. From experiments designed to exploit the distinct nature of surface carrier recombination, we have shown these results to be consistent with established measurements of bulk recombination and surface recombination velocity.

The second part of this thesis deals with the theory and development of the ultrafast optoelectronic switch. This includes the preparation of the GaAs, fabrication of the microstrip line, and measurement techniques. This is followed by a theoretical treatment of the carrier dynamics under picosecond light pulse excitation and a comparison between the predicted and observed height and width of the current pulse. Finally, the means of separately determining the surface and bulk recombination parameters will be discussed.

4.1 Development of Switch Design

There were several stages in the development of the fast opto-electronic switches. The objective of the development was to produce a switch configuration suitable for measuring the fast photoconductivity of Cr:GaAs. Rather than work toward high output voltages, we strove to eliminate artificial limitations on the speed of the switches, so that their temporal response would reflect the inherent speed of the semiconductor material as much as possible.

It was necessary to work in the context of stripline technology in order to provide a well matched circuit at high frequencies to couple into the sampling oscilloscope. The term "stripline" is reserved for a conductive strip imbedded in a dielectric which is sandwiched between two ground planes. A "microstripline" is a metal strip which is separated from a single ground plane by a dielectric medium (see Figure 4.1). Since the strip in a stripline is obscured by the ground planes, the more practical configuration of the switches is the microstripline. Its electrical isolation is not as good as that of the stripline, but accessibility for optical excitation was preeminent in importance. At first, in order to minimize impedance discontinuities in the circuit, an entire microstripline was fabricated from Cr:GaAs. A later design replaced the semiconductor microstripline with commercial stripline materials, and several different approaches were taken to insert the Cr:GaAs chip into the transmission line. Various coaxial arrangements were investigated as well.

The semiconductor microstriplines were constructed from wafers of Cr:GaAs (see Figure 4.2). The size of the chip used was typically 3 x 1 x 0.036 cm. Eutectic gold-germanium was evaporated on the chip to provide a fairly good ohmic contact, and pure gold was evaporated on top to increase the conductivity of the microstripline. The microstripline itself was etched from this metal-

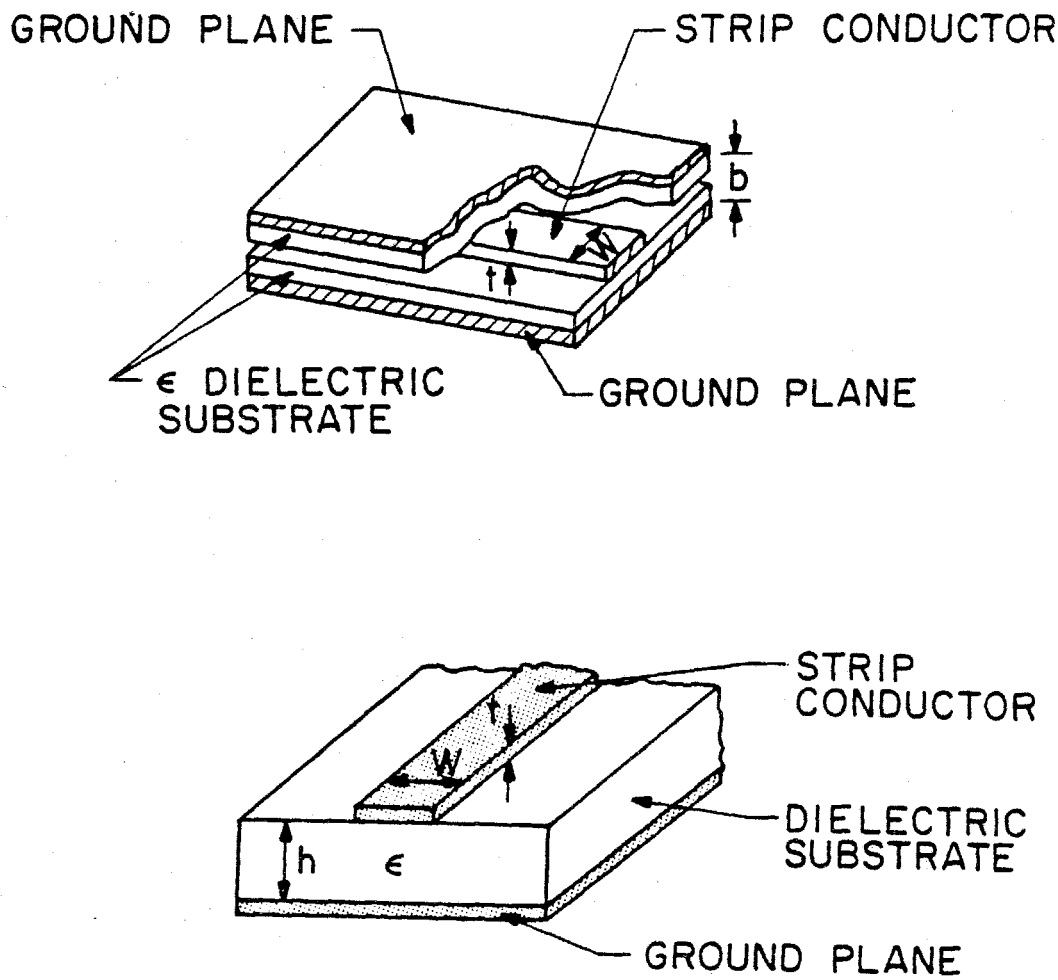

Figure 4.1 A stripline (top), and a microstripline (bottom).

Figure 4.2 An opto-electronic switch with a semiconductor microstripline.

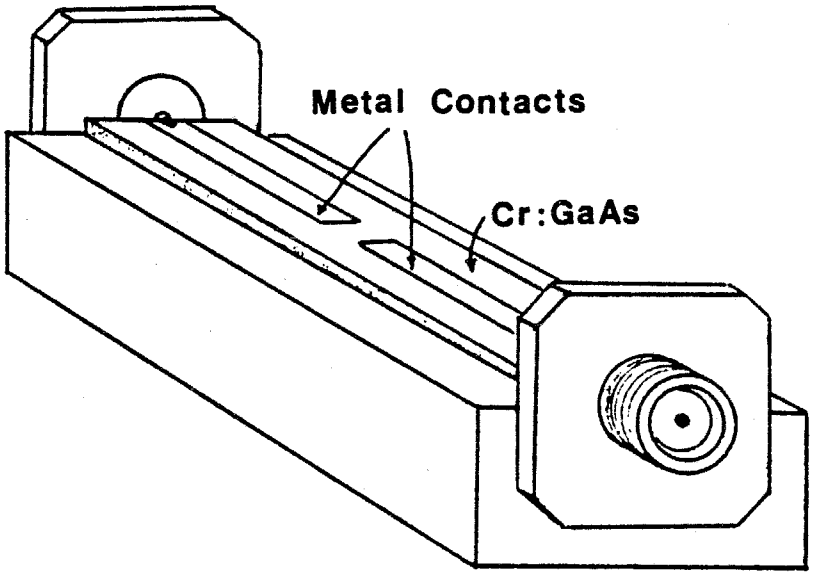

lized layer according to dimensions specified by time-domain reflectometry measurements as well as from published microstrip impedance formulas (see Section 4.2). The Cr:GaAs microstripline was mounted on a gold plated copper block and held in place by OSM miniature connectors with 0.010" diameter terminals [5]. The copper block served as the ground plane of the transmission line. The terminals were soldered to the ends of the transmission line. A gap was etched into the transmission line during fabrication with dimensions of 70, 100, and 400 microns.

The semiconductor microstripline switches were fast (70 psec), but they consumed considerable amounts of Cr:GaAs. Further, it was necessary to cut the wafer to a specified size to match the copper block. A gap caused by a short wafer would generate an impedance discontinuity, and if the wafer were slightly too large, attaching the connectors to the block would shatter the microstripline. For these reasons, it was decided that the microstriplines be constructed from commercially available materials, and that efforts be made to minimize the discontinuities at the connections to the Cr:GaAs chip. The speed of the switches made from commercial substrates was as great as that of the semiconductor substrate switches.

The design of these switches was similar to that of the semiconductor switches (see Figure 4.3). The material consisted of a

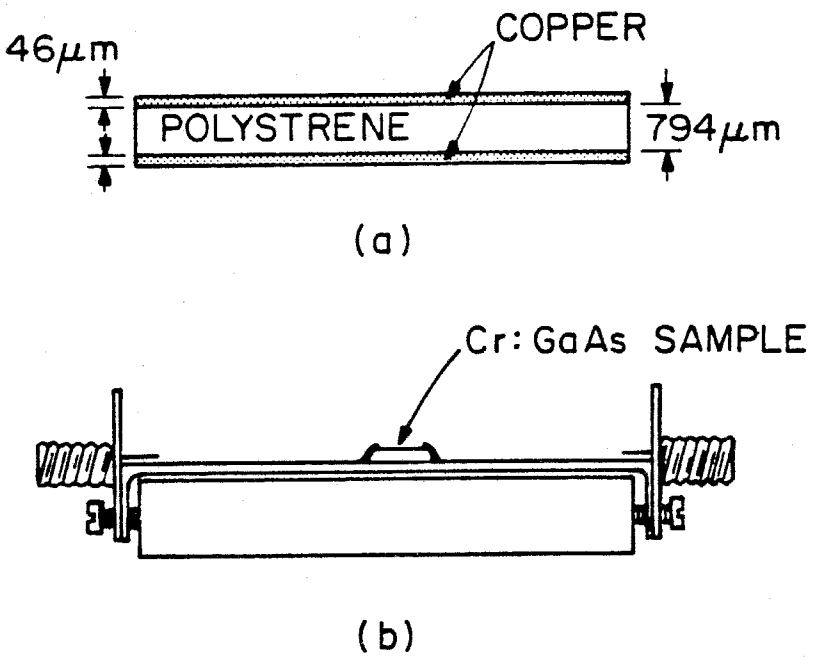

Figure 4.3 An opto-electronic switch with a polystyrene microstrip: (a) the microstrip substrate (b) a side view of the switch

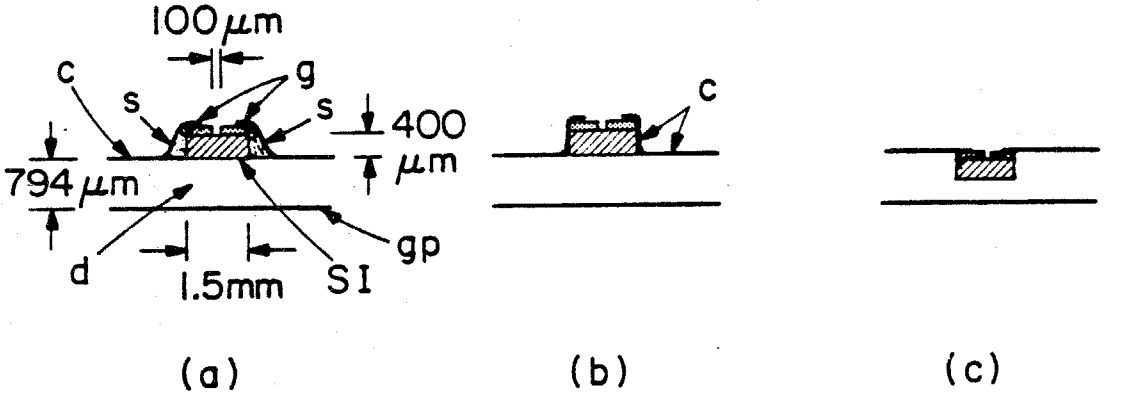

Figure 4.4 Assembly configurations of the Cr:GaAs chip in the polystyrene microstripline: (a) the exposed, (b) the covered, and (c) the buried sample. SI= Cr:GaAs sample, g= metallic contacts, C = copper strip, gp = ground plane, d = dielectric medium, and s = solder or conductive epoxy.

dielectric, most frequently a highly homogeneous polystyrene (1/16" thick), with copper sheets bonded on each side [6]. The support block was 2" long by 3/4" wide, and was constructed from various materials. The composition of the block, now no longer used as a ground plane, had no observable effect on the operation of the switches. A transmission strip with a gap was either cut or photolithographically etched from the top conductive plane. The technique of photo-etching the substrate consisted of spinning photoresist (Shipley 1350J) onto one side of a sheet of stripline material and exposing the resist through a mask. The photoresist was developed, more photoresist was painted on the back of the substrate to protect the ground plane, and the substrate was etched in a hot saturated solution of either ferric chloride or ammonium persulfate. OSM miniature connectors were attached to the ends of the block; their terminals were 0.050" gold plated tabs. The terminals were soldered to the ends of the striplines. To ensure good ground plane continuity, the ends of the ground plane were folded over on the block and held in place with the ground flanges of the miniature connectors. Wafers of Cr:GaAs were prepared (see Section 4.3) with metallic contacts of Au, Au-Ge, Au-Zn, In, or Cr. The contacts were prepared with 75 micron gaps. Then the wafers were cleaved into appropriately sized chips (1.9 x 1.9 mm) for mounting on the gap in the transmission strips.

Several methods of mounting the chips in the microstripline were investigated, all with an effort at reducing the impedance discontinuities of the line (Figure 4.4). Although the illuminated resistance of the Cr:GaAs chip never dropped below a few $k\Omega$, it was important to minimize the impedance mismatch in the line from the gap to the 50Ω sampling head. In most of the cases, the chips were mounted directly on top of the gap in the line, and the electrical contacts were made with indium-silver solder (90% In, 10% Ag) or with conductive (gold or silver) epoxy (Fig 4.4a). In some switches, the transmission line strips were peeled back from the substrate and used to establish direct contact to the chip (Fig 4.4b). In a few cases, the chip was buried in a rectangular pit cut into the dielectric. The strips of the transmission line were then soldered directly onto the contacts (Fig 4.4c). The measures that were taken beyond the first method described had no noticeable effect on the speed of the switches. One possible explanation for this might lie in the 25 picosecond resolution of the sampling system, which corresponds to 4 mm of propagation length. Since any untreated discontinuity in the impedance at the chip could not have been larger than 1 mm, it probably never would have been seen by the detection system. The first mounting technique was the method of choice, being easiest to perform, and allowing convenient chip replacement.

Another switch design was the coaxial switch, patterned after a fast photodiode package developed by McCall [7]. This design (Figure 4.5) featured a Mylar sheet capacitor on the biased end of the chip. The other end of the chip was mounted on the terminal of a miniature connector. It was hoped that the low impedance source of charge would provide a ready supply of current; however, there was no improvement over the switch in Figure 4.4a. The resistance of the chip was always too high to make use of the low impedance input.

4.2 The Microstrip Line

The most fundamental attribute of a high speed transmission system of electrical signals is the impedance. The impedance of such a system is the ratio of voltage to current in a traveling wave. Wherever an impedance discontinuity appears in a transmission system, the boundary conditions of electric field and current conservation cannot be satisfied without the creation of a reflected wave at the discontinuity. In a poorly impedance matched system, the superposition of reflected signals at a detector does not exhibit the true nature of the original signal. For example, a short pulse would appear broad due to the presence of multiply reflected and delayed pulses that arise at the impedance discontinuities. It is important, therefore, to design a transmission system with a uniform impedance in order to facilitate the accurate interpretation

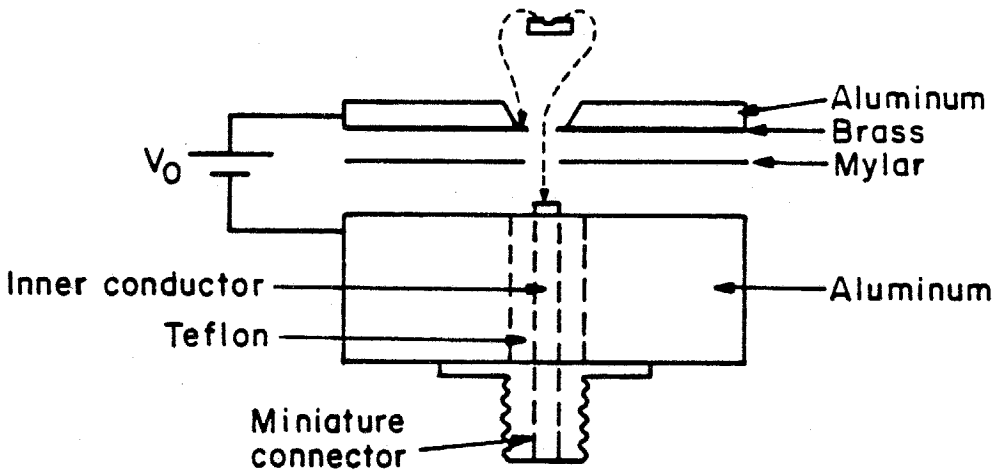

Figure 4.5 A coaxial switching unit.

of the transmitted signal.

The sampling system has a characteristic impedance of 50 ohms. This determines the impedance of the microstripline, and the first task in developing the device is to determine the dimensions needed to fabricate a 50 ohm microstripline. A very rough estimate of the impedance of a microstripline is $Z=h/(c\varepsilon w)$, where c is the speed of light, ε is the dielectric constant, and h and w are shown in Figure 4.1. This formula is only good for $w>>h$; in our case, we need a more sophisticated analysis. There is a wealth of data in the literature; both theoretical and empirical expressions have been developed to describe the impedance of a microstripline given its dimensions, and vice versa [For examples, see Refs. 8-11]. Unfortunately, there is very little agreement between any of these sources; there is a range of a factor of two in which the results lie [12]. For our experiment, we used a time-domain reflectometer to determine the impedance of microstrips that were fabricated according to the rough consensus of the literature.

In a time domain reflectometer (TDR), a fast risetime voltage pulse is launched into an electrical system from a 50 ohm cable. If there is any impedance discontinuity in the system, the resulting reflection returns to the TDR, and is displayed on the voltage step. From the height of the reflected signal, and from its delay relative to the voltage step, the magnitude, sign, and location of the im-

pedance discontinuity may be determined (Figure 4.6).

We constructed a number of microstriplines using rough estimates of the correct strip width. From TDR measurements of these microstriplines, we interpolated to determine the correct strip width for a $50\,\Omega$ device. This width for the polystyrene microstripline was 0.188 cm; for the Cr:GaAs microstripline, the correct width was .036 cm. It turned out that Kaupp's empirical formula [11] showed excellent agreement with our experimental data. His expression is

$$\frac{w}{h}=1.25\left|\frac{5.97}{\exp(z\sqrt{\varepsilon+1.41}/87)}-\frac{t}{h}\right| \qquad 4.1$$

where the symbols are defined in Figure 4.1.

Even an impedance matched microstripline cannot transmit high speed signals without distortion. Sources of this distortion include the frequency dependence of the group velocity, the high frequency loss tangent of the dielectric, and the ohmic loss of the conductor due to decreasing skin depth at high frequencies [13-15].

When switch measurements were taken in a magnetic field (See Section 6.3), the oscilloscope sampling head was placed at a distance from the switch. This was done to avoid any influence of the high magnetic field on the components within the sampling

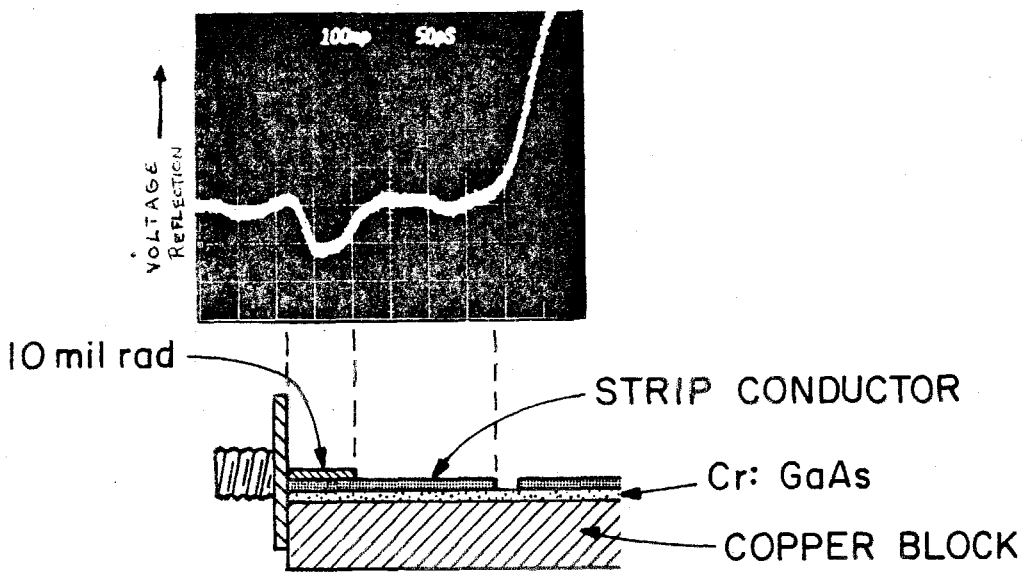

Figure 4.6a) Time domain reflectometer display of a semiconductor microstripline. The microstripline is connected on the left to a 50 ohm line.

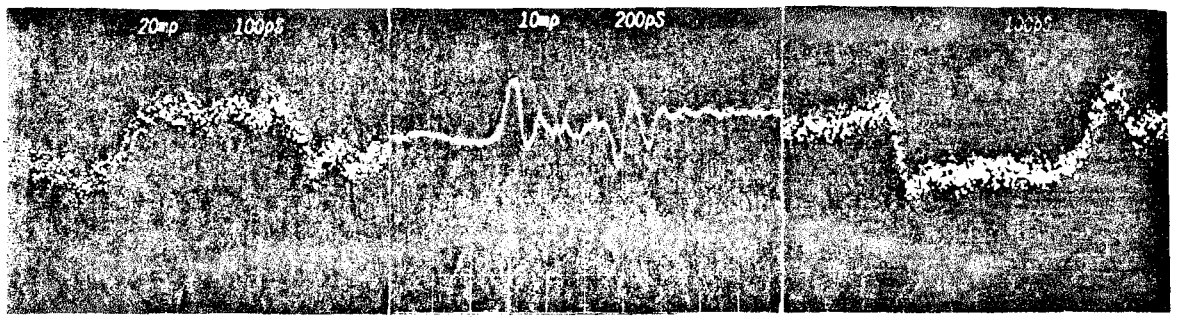

w = 1.63mm
z = 53Ω

w = 1.88mm
z = 50Ω

w = 2.03mm
z = 47Ω

b) Voltage reflection (vertical axis) from impedance discontinuities along a polystyrene microstripline. The discontinuities occur at the transitions between the line and the connectors.

head. The interposition of a high-speed signal cable between the switch and the sampling head resulted in further signal dispersion over the microstripline dispersion. Rather than calculate the overall bandwidth of the microstripline and signal cable, we measured the increase of the width of a fast pulse upon passage through a microstripline without a gap and then through the cable. We produced the fast pulse by differentiating the fast risetime step from the time domain reflectometer pulse generator. This fast pulse was a small amplitude pulse with a full width at half-maximum of 40 picoseconds. The risetime of the sampling head was 25 picoseconds. The pulse broadened to 43 picoseconds upon passage through the transmission line; assuming that the bandwidths are Gaussian, and the convolutions are quadratic, the risetime of the entire system was 30 picoseconds. We used this figure in the curve fitting described in Chapter 6.

4.3 Surface Preparations

The high absorption coefficient of Cr:GaAs ($4.3\times10^{4} cm^{-1}$ [22]) at the visible wavelength of the mode locked dye laser implies that photocarrier lifetimes will be greatly affected by the conditions at the surface of the semiconductor. In order to explore the effects of surface preparation on the photocarrier lifetime, switches with various surface preparations were constructed. This discussion of surface preparation techniques applies specifically to Cr:GaAs

chips in switches with polystyrene microstriplines. In all, over sixty switches were investigated.

The tests performed on these switches measured the surface recombination velocity s; we investigated the relationship between various surface preparations and the resulting observed value of s. Surface recombination velocity is defined as the observed constant of proportionality relating the rate of carrier recombination at the surface (carriers per unit time per unit area) with the carrier concentration at the surface (carriers per unit volume). The magnitude of s is determined by the conditions at the surface of the material, including the lattice termination, lattice defects, and adsorbed impurities. The concept of surface recombination will be treated in more detail in Section 5.3.

In the early stages of switch production, the technique of chip preparation was a typical photolithographic method. After the surface of the chip was treated according to some prescription, a metal or metal alloy, such as gold, gold-germanium, or gold-zinc was evaporated onto the entire wafer. The wafer was spun with positive photoresist (Shipley 1350J), and exposed with UV light through a mask. The mask consisted of an array of slits, 75 microns wide. After development, the wafer was immersed in a gold etch solution ($KI:I_2:H_2O$=275:150:250 by weight), and the exposed metal regions were etched away to form 75 micron gaps in the contacts. The

wafer was then alloyed in a hydrogen atmosphere at 400 °C to establish a good electrical contact and strong mechanical bond between the metal and the semiconductor. The wafer was cleaved into appropriately sized chips for the switches, soldered to the stripline, and then tested. Some of the results of these tests are tabulated in [12]. There was virtually no relationship between the surface preparation and the speed of the device. It was hoped that by preparing the surface in such a way as to increase the surface recombination velocity, the photocarrier lifetime would decrease accordingly. Such results were not seen in switches with GaAs crystals which were prepared by the above technique.

The difficulty in demonstrating a connection between the surface conditions and carrier lifetime lay in the sample preparation. The gold etch not only removed the metallic contact over the gap, it attacked the Cr:GaAs as well. Further, the chips were heated in the alloying oven, which promoted chemical reactions between the Cr:GaAs and any adsorbed impurities, as well as causing the sublimation of arsenic from the surface. So, regardless of the surface preparation established on the chip prior to switch fabrication, the surface conditions were determined by the gold etch and the heat of alloying oven. It was necessary to develop a technique of applying metallic contacts to the chip without etches, and preferably without the application of any coating, such as photoresist. Fur-

ther, the electrical and mechanical bond between the Cr:GaAs and evaporated metal would have to be of high quality without alloying. It was found that chromium satisfied the requirements imposed on the contact material. The non-alloyed Cr:GaAs-chromium contact provided the highest output signal for the switches, and was extremely durable. An evaporation mask was developed which strung 75 micron stainless steel wires across the chip, with sufficiently close contact to the chip that no evaporation shadowing took place. The result was a clean gap in the contacts with minimal contamination of the surface. Indium-silver solder was used initially to bond the chip to the stripline; to eliminate that source of surface heating, conductive epoxies were then used exclusively. Magnetophotoconductivity tests showed that the surface recombination velocity was determined by the initial surface preparation; there was good agreement between this data and luminescence studies which determined the surface recombination velocity independently [16].

The surface recombination velocity s in Cr:GaAs can be varied from 450 cm/sec to more than 10^6 cm/sec, by means of appropriate surface preparations. s has been reduced to 400-500 cm/sec when the surface is passivated by an epitaxially grown layer of $Al_xGa_{1-x}As$. Low values of s are also obtained with chemical solutions, such as one causing the chemisorption of ruthenium ions [17] ($s = 3.5\times10^4$) , and etches, such as solutions of citric acid [16]

or phosphoric acid [18] ($s \approx 5 \times 10^5$). The highest surface recombination velocities are obtained from mechanical polishing with abrasive grits ($s \gtrsim 10^6$). The various surface preparations used in our experiments include the AlGaAs passivating layer grown with molecular beam epitaxy [19], a citric acid etch (saturated citric acid in water: nitric acid: water= 2:1:2 by volume) [16], and mechanical polishing (3 micron alumina grit applied until a matte finish is obtained).

4.4 The Experimental Set-up for Switch Measurements

The experimental set-up is shown in Figure 4.7. A chip of Cr:GaAs has metallic contacts evaporated on its surface. The chip is mounted on a microstripline, and a voltage is applied across a gap in the metallic contacts. Ordinarily there is very little current flow due to the high resistivity of the material. When the gap is illuminated with a picosecond light pulse, photocarriers are created in the gap, and current flows for the duration of the photocarriers' existence.

The detection system for measuring the current waveform consisted of a Tektronix 7904/ 7S11-7T11 sampling oscilloscope system with a 25 picosecond risetime sampling head, the S-4 or the S-6. The sampling system required a trigger to arrive 80 nanoseconds before the signal. In order to minimize jitter from

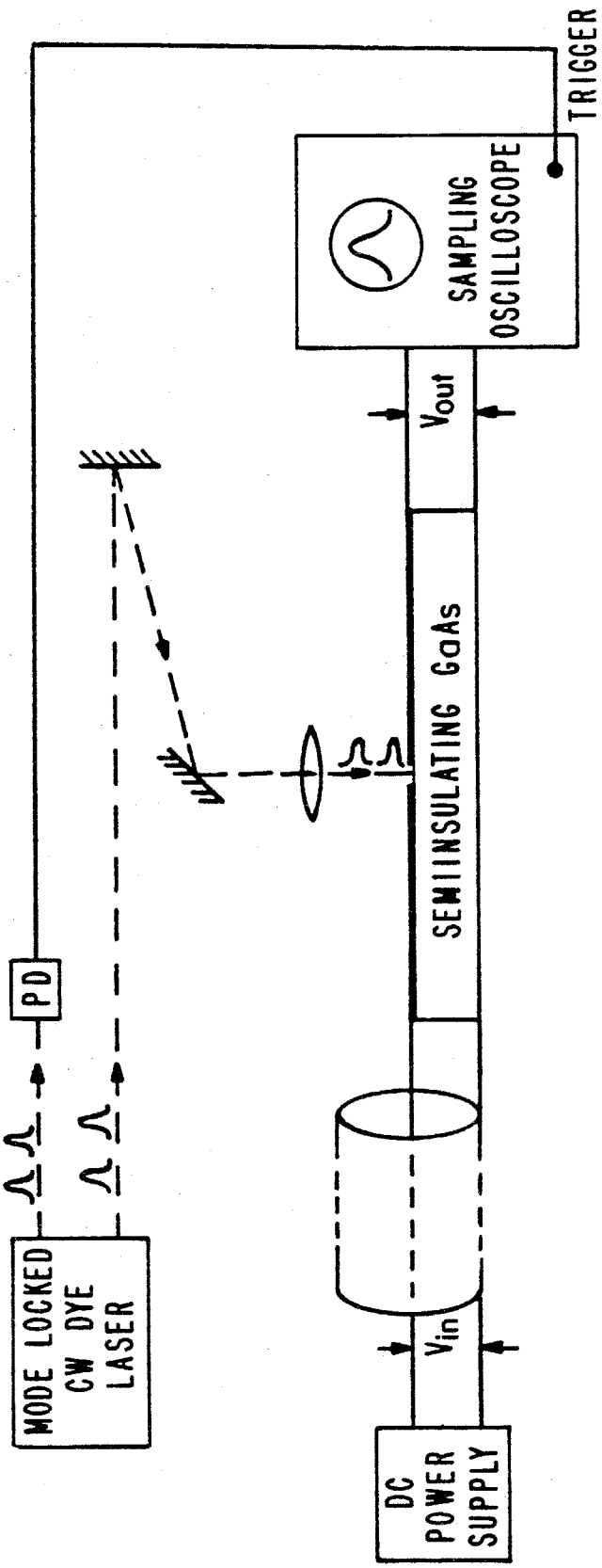

Figure 4.7 Experimental set-up for Cr:GaAs photoconductive impulse response measurements. PD is a fast photodetector. The two pulse trains are mutually synchronized.

pulse to pulse, we triggered the oscilloscope with a current pulse from a photodiode which detected a portion of the laser pulse. The remainder of the light pulse traveled down an 80 nanosecond delay line in air before reaching the switch. Miniature high-speed connectors and semi-rigid cable were used in carrying the signal from the switch to the sampling head, and all connections were made as short as possible. The data from the sampling system was stored digitally on the Nicolet 1174 signal averager. The sweep of the sampling head was controlled by the signal averager, and the voltage of the vertical signal of the oscilloscope was stored into memory. Thus, the inherently large noise of the sampling head was averaged away, and the signal could be stored for processing. In this manner, many signals could be stored on magnetic tape for processing on Caltech's IBM 370 computer.

4.5 Experimental Photoconductivity Results

We constructed switches according to the method described above. The switches were tested by applying an electric field of 4×10^3 v/cm to one end, illuminating the gap with a picosecond pulse from the dye laser, and measuring the current flow with a 25 picosecond sampling head. A typical result of one of the fastest switches is shown in Figure 4.8. The risetime is limited by the sampling head, and the falltime by the effective photocarrier lifetime

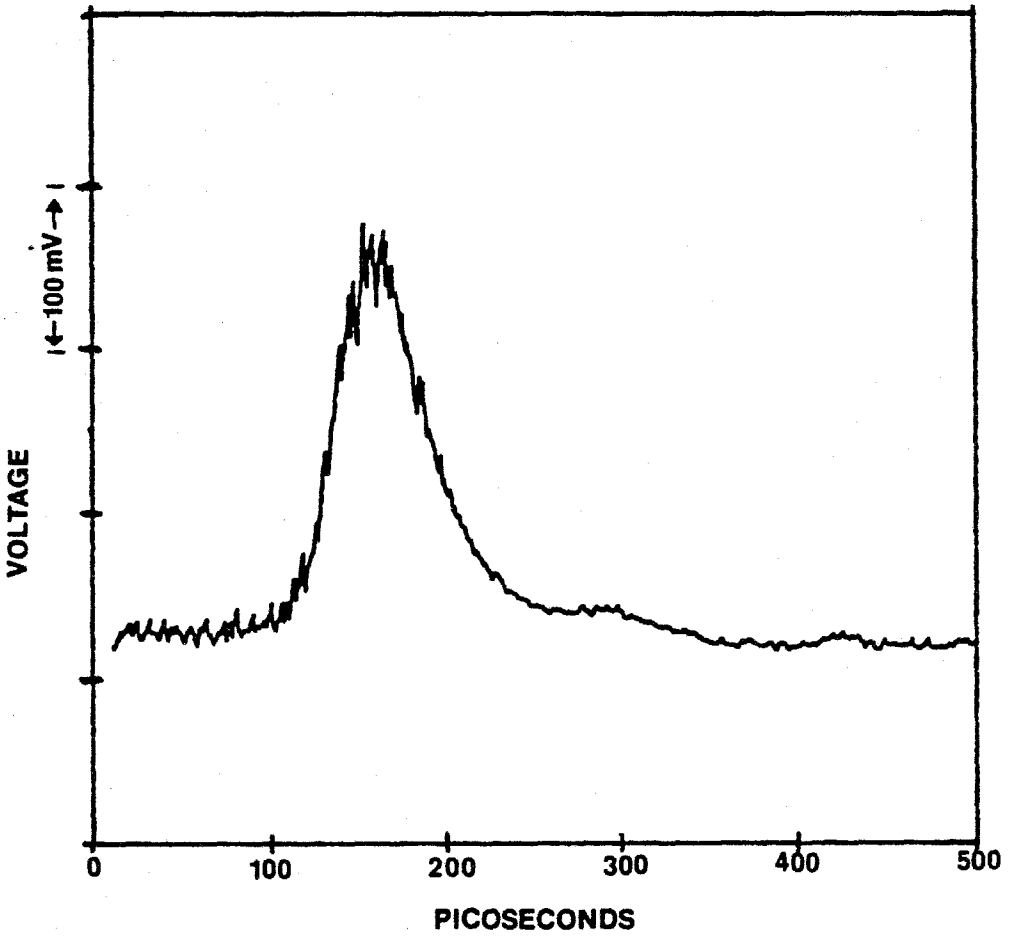

Figure 4.8 Output of an opto-electronic switch upon illumination by a picosecond pulse.

in the Cr:GaAs. This photocarrier lifetime is determined by both the bulk recombination rate and the surface recombination velocity.

Ideally, the bulk recombination rate should not vary too greatly from one sample of Cr:GaAs to another. If this were the case, the surface conditions could be altered on different samples, and the effects of these alterations could be investigated with the knowledge that the other material parameters were constant. Unfortunately, this situation does not always exist; a common problem of doing measurements on Cr:GaAs is the variability of specimens obtained from different growth techniques, or even from different locations in the same ingot [20]. Our Cr:GaAs was generally obtained from Crystal Specialties Inc. [21]. The measurements done on these samples indicated fairly constant material characteristics. The variability that we saw in several ingots, and many different wafers from these ingots implies that the accuracy of our results is about 10% within a single wafer, and about 30% for Cr:GaAs as a whole.

The photocarrier lifetimes of carefully made switches depended strongly on the surface preparation. The lifetimes were measured according to the 1/e point on the current decay curve. This time was deconvolved with the response time of the entire electrical system. The fastest switches were constructed using the early

technique of construction; thus the gold etch in the presence of the contacts coming into solution provided the most active surface for recombination. The photocarrier lifetime was about 70 picoseconds. The switches whose surfaces were prepared by mechanical polishing showed the next shortest lifetime of 80 picoseconds. The citric acid passivating etch reduced the surface recombination velocity to the point where the lifetime was 100 picoseconds.

The switch with the most passivated surface, that with the GaAlAs cap, was the slowest of all, with a 450 picosecond lifetime. This last switch displayed the properties of pure GaAs rather than Cr:GaAs. The reason for this was that the passivating properties of GaAlAs only appear at an epitaxial interface. If the GaAlAs were grown directly on the Cr:GaAs substrate, the recombination at the interface would reflect the lattice defects and adsorbed impurities of the sawn, lapped, polished, and inevitably contaminated surface of the Cr:GaAs, rather than the Cr:GaAs-GaAlAs interface. So, an epitaxial layer of pure GaAs was grown on the substrate, and then the GaAlAs layer was grown on top of that. It was not practical to grow Cr:GaAs instead of the pure material. Thus, the measurements of this switch provided data on the effect of chromium in GaAs as a recombination center.

Some switches were constructed using O:GaAs, where oxygen

is used as a recombination center instead of chromium. There was no noticeable difference between the behavior of the oxygen doped material and Cr:GaAs. Experiments were done with semi-insulating Fe:InP; The photocarriers showed comparable lifetimes at a passivated surface (100 picoseconds), but the most significant property of the InP switch was its large throughput. We have defined throughput as the ratio of input voltage to peak output voltage measured on a 50 ohm load. Typical throughputs for Cr:GaAs switches were 0.1% for gold and gold alloy contacts, and 0.8% for chromium contacts, constant over a broad range of input voltage. Throughputs for InP switches were typically four or five percent, making them attractive candidates for fast current pulse sources.

4.6 Conclusion

Opto-electronic switches can have pulse widths of less than 100 picoseconds. As a result, they have at least three major applications.

(1) First, they are very fast photodetectors; they are among the fastest detectors available. They are simple, have large sensitive areas, and have a fairly good signal to noise ratio (40 dB). They are not very sensitive, however, generating 30 microamps per watt of incident optical power.

(2) A second application of these switches is as a fast current

source to drive devices such as diode lasers (See Figure 4.9). In order to reduce impedance matching problems between the 50 ohm line and a 2-3 ohm diode laser, the switch and laser could be integrated on a single chip. Nevertheless, detector limited pulses (<200 psec.) have been observed with our switches connected to Hitachi diode lasers through 50 ohm lines. Accurate temporal measurements can be done by mixing the dye laser pulse with the much weaker diode laser pulse in a non-linear crystal. This would be more effective than performing SHG on the diode laser pulse, since the greater power and higher resolution of the dye laser pulse would make nonlinear measurements easier and more accurate.

(3) Finally, and most importantly for this discussion, these switches allow measurements of the material parameters in semiconductors. By investigating the overall photocarrier lifetimes under different conditions, a quantitative determination of the carrier recombination parameters can be undertaken.

We have constructed photoconductive switches that are capable of producing current pulses that reflect the photocarrier lifetime in the constituent semiconductor. Such lifetimes are determined in the semiconductor by surface and bulk carrier recombination. There was an explicit dependence of photocarrier lifetime on surface preparation, and evidence of the effect of chromium on the bulk recombination rate. It is now necessary to investigate these

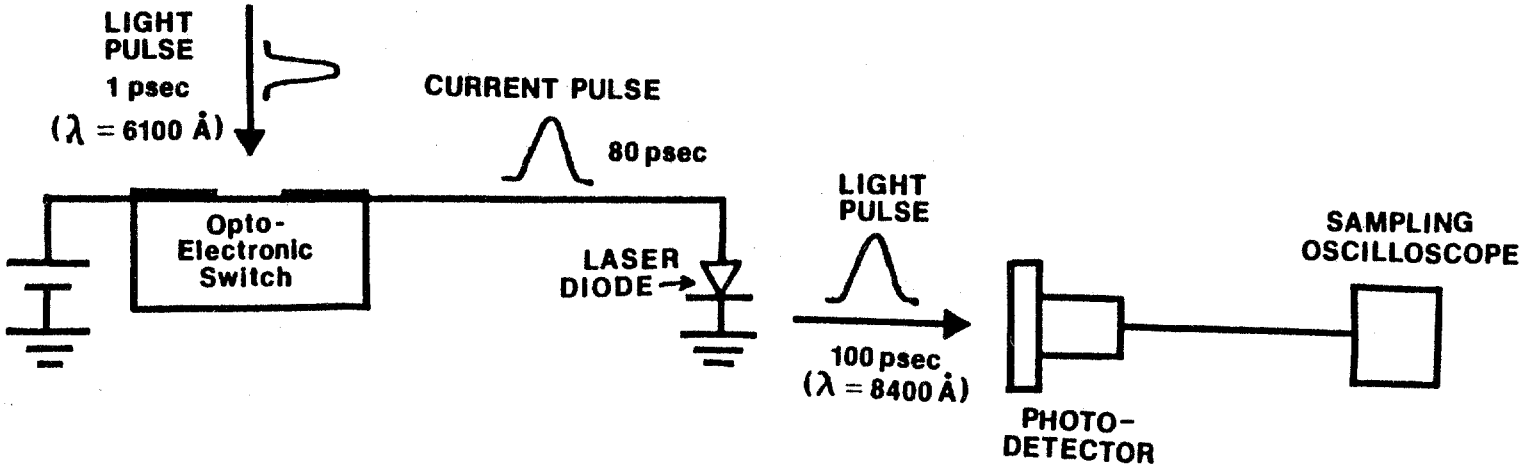

Figure 4.9 The opto-electronic switch as a laser driver.

phenomena in Cr:GaAs to establish the analytical dependence of photocarrier lifetime on the surface and bulk recombination parameters.

Chapter 5

The Theory of Ultrafast Photoconductivity of Semi-insulating Gallium Arsenide

5.0 Introduction

In order to interpret the behavior of the photoconductive switches, we need to examine the processes that determine the lifetime of photocarriers. In Cr:GaAs, electron-hole pairs recombine through direct band to band transitions, through Auger processes, and through intermediate interband states. These intermediate states can be present in the form of recombination center impurities, or as states that arise in the forbidden gap due to the lattice termination at the surface. The carriers migrate through the semiconductor due to the electric field as well as through diffusion.

In this chapter, the different recombination processes will be investigated to form estimates of their magnitude. Further, a diffusion equation describing the dynamics of the photocarriers will be developed which includes the effects of the electric field, ambipolar diffusion, bulk recombination, and surface recombination velocity. Using known values of recombination rates, we will compare the results of this analysis with the experimental photocon-

ductivity data that we have obtained.

5.1 Carrier Recombination in the Bulk

The resistivity of Cr:GaAs can be very high; it is generally 10^8 ohm-cm. It is possible to calculate the concentration of thermally excited carriers from simple considerations of the Fermi distribution of electrons and holes in the material. The concentrations of electrons and holes are given by the expressions

$$n_0 = 2\left[\frac{2\pi m_e^* kT}{h^2}\right]^{3/2} e^{-(E_c - E_f)/kT}$$

$$p_0 = 2\left[\frac{2\pi m_h^* kT}{h^2}\right]^{3/2} e^{-(E_f - E_v)/kT} \qquad 5.1$$

where m_i^* are the effective masses of electrons and holes. These effective masses are $m_e^* = 0.07\ m_0$, and m_h^* is $0.5\ m_0$. E_c, E_f, and E_v are the energies of the conduction band, the Fermi level and the valence band of the semiconductor. The band gap is 1.43 eV, and the Fermi level is generally taken to be 0.74 eV above the valence band. The Fermi level is very nearly in the center of the semiconductor, so the calculations proceed directly to obtain

$$n_0 = 5\times10^6 cm^{-3}$$

$$p_0 = 1\times10^7 cm^{-3} \qquad 5.2$$

as approximate values for the free carrier concentration. The resulting bulk resistivity is $\rho=\frac{1}{ne\mu_n+pe\mu_p}$. We take the electron mobility to be $3000cm^2/V-sec$, and the hole mobility to be $170cm^2/v-sec$. Thus, $\rho=5\times10^8$ ohm-cm, within the observed range. Our photoexcitation carrier density is

$$n=p=\frac{\Phi\alpha}{laser\ spot\ area} \qquad 5.3$$

where $\Phi=10^8$ is the number of photons in the laser pulse, and $\alpha=$ 1/2300 angstroms is the absorption coefficient of GaAs at 6100 angstroms. Thus, the photocarrier density is approximately $10^{14}cm^{-3}$. We see that the equilibrium carrier concentration is negligible compared to the optically excited population, so only these carriers need to be considered as participants in recombination.

Recombination takes place through unassisted band to band transitions (including Auger transitions) and at recombination centers such as oxygen and chromium. The carrier lifetime due to the former process has been estimated to be about 3 nanoseconds [22]. This process alone is too slow to be responsible for the fast bulk recombination rate observed in our Cr:GaAs switches (τ = 250 psec., see Chapter 6); the rate must be strongly determined by the recombination centers.

As we saw above, the equilibrium concentration of free car-

riers is negligible compared to the photoexcited population created by the picosecond light pulse. Consequently, the initial carrier population, composed almost exclusively of photoexcited electron-hole pairs, is made up of an equal number of electrons and holes. The band to band recombination rate for electrons, for example, is then

$$\frac{\partial n}{\partial t} = -Cnp = -Cn^2 \qquad 5.4$$

A result of this situation would be a dependence of carrier lifetime on the initial excitation level.

$$n(t) = \frac{1}{Ct + 1/n_0} \qquad 5.5$$

where n_0 is the initial carrier concentration. We saw no dependence of decay time on the intensity of the picosecond pulse, leading us to conclude that the band to band process of recombination does not play a significant role in carrier lifetime determination. We then must consider the effect of the chromium dopant as a recombination center in the material.

Deep levels in semiconductors, such as chromium in GaAs, increase the rate of carrier recombination. This can be seen through an uncertainty principle argument by recognizing that an electron, trapped and highly localized by a recombination center, has a

correspondingly broad range in momentum-space. As a result, a hole with a relatively narrow wavevector may recombine with the trapped electron; the momentum conservation criterion of the recombination process is readily met without the necessity of creating a phonon.

The concentration of chromium in Cr:GaAs is highly variable, even within a single wafer of the material [23]. Much of this variation is due to a large solubility difference of chromium in the liquid and solid states of GaAs; as the crystal is grown, chromium migrates toward the liquid portion of the GaAs. Thus, the regions that solidify last have the highest concentrations of chromium, and the first regions to solidify have the least. As a result, the chromium concentration can vary from 10^{16} to more than $10^{17} atoms/cm^3$. For our analysis, we will assume a concentration of $10^{17} atoms/cm^3$.

The recombination of carriers through a recombination center takes place through a two step process. First, an unionized center captures a carrier, an electron, for example. Now the center is ionized, and the capture of a hole is greatly enhanced by the Coulomb attractive force. This second step will occur almost immediately after the first step. Thus, the limiting process in the recombination, the unionized capture, will establish the recombination rate at the centers. Thus, the recombination rate will depend on the product of the concentration of the species to be captured, and the

concentration of the chromium.

$$\frac{\partial n}{\partial t}=\sigma v_{th} n N \qquad 5.6$$

where σ is the unionized capture cross section, v_{th} is the thermal velocity, and N is the chromium concentration. Thus the decay time is

$$\tau=\frac{1}{\sigma v_{th} N} \qquad 5.7$$

Note that this decay time is independent of the initial electron concentration, which is consistent with our observation. Using typical values for the cross section $\sigma=3\times10^{-17}cm^2$ [24], and thermal velocity $v=4.5\times10^7$ cm/sec, we obtain a recombination lifetime of 8 nanoseconds. This rate is too low to explain the bulk recombination rate observed in Cr:GaAs. Either the recombination rate through chromium is higher than we just calculated, or there are other recombination centers such as oxygen in the material, or both. Since we did not see any dependence of carrier lifetime on the excitation intensity, we must assume that the dominant recombination process is monomolecular, i.e., through a recombination center.

The GaAlAs switch was identical to the other polystyrene microstripline switches, except that the gap of the GaAs chip was

capped first with an epitaxially grown layer of pure GaAs, and then with another layer of GaAlAs for surface passivation (Figure 5.1)[19] We chose the concentration of aluminum in the GaAlAs to be sufficiently high (55%) to be transparent to the 6150 angstrom light pulse. The interface between the pure GaAs and the GaAlAs served as the photosensitive region. The concentration of chromium in the pure GaAs layer was estimated to be less than $10^{14} atoms/cm^3$ at the very most. Further, the observed decay time was 450 picoseconds, the longest observed. It might be expected, then, that the observed recombination at the highly passivated GaAs-GaAlAs interface would be associated with unassisted band to band transitions, and not be due to recombination center effects. This is not a reliable assumption, however. The GaAlAs cap was oxygen doped semiinsulating material. The passivating layer was made semiinsulating in order to eliminate current leakage through that layer. The diffusion coefficient of oxygen at the temperatures of molecular beam epitaxial growth is roughly $10^{-13} cm^2/sec$ [19]. The top layer growth took approximately one hour; the diffusion length of oxygen into the originally undoped GaAs would have been approximately 2000 angstroms. So, a significant portion of the top of the GaAs sensitive layer was oxygen doped material; recombination processes would be strongly affected by the presence of oxygen as a recombination center. Thus, we can assume only that the longer decay time in the GaAlAs switch was due to a lower concentration

Figure 5.1

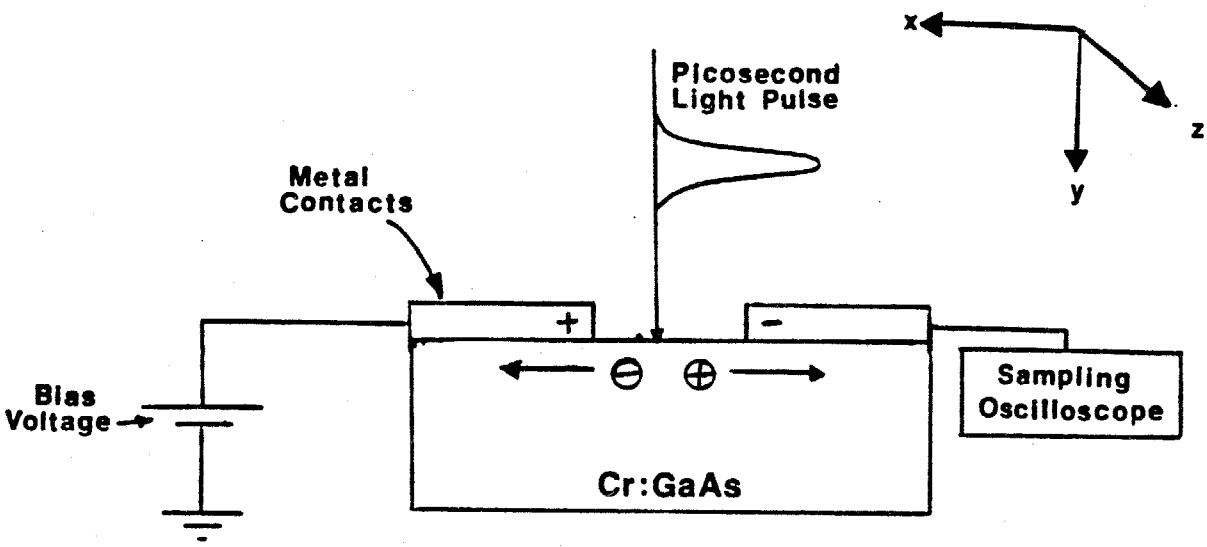

Geometry of the Opto-electronic Switch

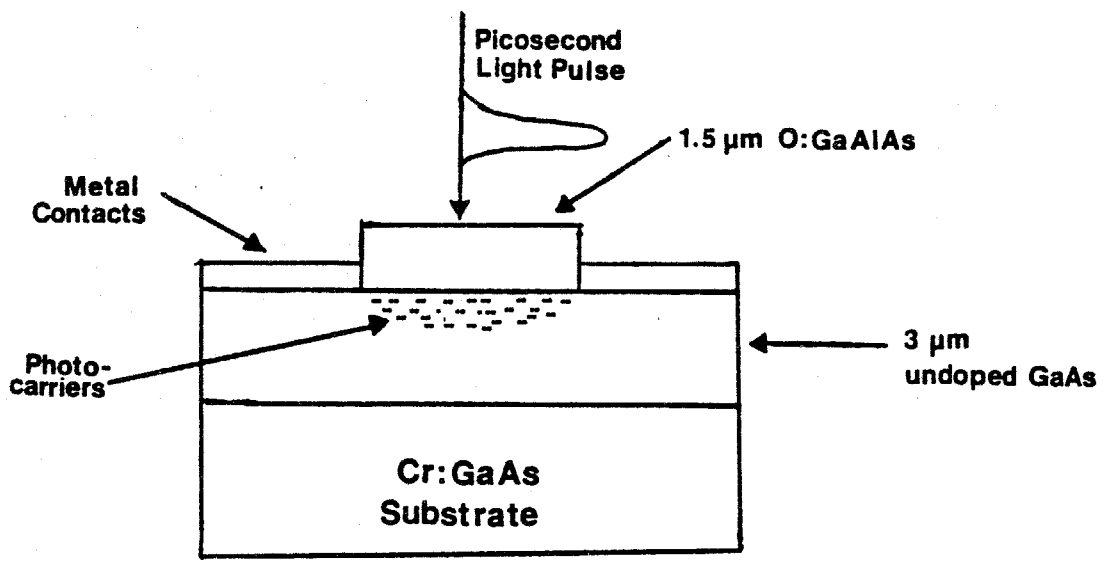

The Heterostructure Opto-electronic Switch

of recombination centers, including those at the interface, and not to their complete absence.

5.2 Surface Recombination

Surface recombination of free carriers in GaAs is a frequent impediment to successful electronic device fabrication. The free surface of GaAs acts as a powerful recombination agent for a number of reasons. The surface of GaAs, as well as that of any other material, necessarily consists of a lattice termination. The electronic states of a semiconductor are segregated into bands as a result of the periodicity of the crystal lattice; where this periodicity is disrupted, such as at the surface, electronic states may appear in the middle of the band. It is through these states that enhanced electron-hole recombination may take place. Further, whatever impurities there are at the surface of the material can act as recombination centers. Moreover, GaAs does not have a natural passivating oxide, as silicon does, for example. The arsenic sublimes from the surface, upsetting the stoichiometric balance, which further perturbs the lattice. Hence, the surface of materials, especially that of GaAs, can be the site of interband states which aid in the recombination of photocarriers.

Surface traps in GaAs immobilize large numbers of electrons at the surface of the material. As a result, a space charge region is

created in a shallow layer near the surface which consists of a population of holes coulombically attracted to the trapped electrons. The thickness of this layer has been found to be on the order of tens of angstroms [16], whereas the typical extent of the photocarrier population in our switches is roughly a diffusion length, or 5000 angstroms. Thus, the space charge effect is essentially a surface phenomenon in our experiment. There will be an enhanced electron recombination rate at the surface due to the increased free hole concentration, and a reduced hole recombination rate for the same reason. Due to the greater electron mobility compared to hole mobility ($\mu_e/\mu_h = 20$), the Cr:GaAs can be treated as an n-type material; the altered recombination rates at the surface have a net effect of decreasing the conductivity at the surface. The phenomenological surface recombination velocity is a combination of the effects of the space charge region and recombination centers at the surface. Photoconductivity and luminescence measurements taken over a broad spectrum can discriminate between these two contributions by demonstrating a wavelength shift of the luminescence and photoconductivity peaks toward longer wavelengths [16]. Since our measurements were all taken within a narrow band of excitation wavelengths well above the energy gap, we were unable to resolve any of the details of the two surface recombination processes. We did obtain results, which, when interpreted in the context of phenomenological surface recombination

velocity, agree well with these luminescence studies.

The usual analytic description of surface recombination velocity begins by assuming that there are ρ recombination centers per unit area in a thin layer near the surface of a material, with some capture cross section σ. Assume that a material has a uniform carrier concentration n throughout its volume, and that $\sigma=0$. If a non-zero σ is suddenly "turned on", carrier recombination will begin at the surface, and according to the diffusion coefficient D, there will be a current flow toward the surface. Specifically, this particle current per unit area just beneath the surface can be expressed

$$-D\frac{\partial n}{\partial y}(y=0)=n\cdot\sigma v_{th}\rho \qquad 5.8$$

where v_{th} is the thermal velocity of carriers [25]. We see that the product $\sigma v_{th}\rho$ is equal to the surface velocity, and that this product is a constant of the material specimen at a given temperature. This constant is identical to the surface recombination velocity s defined earlier; Equation (5.8) is used as a boundary condition for differential equations of free carrier dynamics. A typical value of s for GaAs is 10^6 cm/sec; generally there is assumed to be one recombination center per atom at the lattice termination. Consequently, the magnitude of the capture cross section σ is roughly $10^{-18}cm^2$.

5.3 A Diffusion Model of the Switch

Photocarriers created in Cr:GaAs initially follow the profile of $e^{-\alpha y}$, where α is the optical absorption coefficient of the material, and y is the distance into the medium. The carriers recombine at the surface and throughout the bulk, while diffusion acts to smooth out the distribution. We assume a monomolecular bulk recombination rate according to Section 5.1. The geometry of this analysis is shown in Figure 5.1. The currents follow the continuity equations

$$\frac{\partial n}{\partial t}=-\nabla\cdot\vec{j}-\frac{n}{\tau} \qquad 5.9$$

$$\vec{j}=-D\nabla n+\mu\vec{E} \qquad 5.10$$

Combining the two above equations gives the differential equation for the charges

$$\frac{\partial n}{\partial t}=D\nabla^2 n-\frac{n}{\tau} \qquad 5.11$$

This equation is subject to the boundary conditions

$$n(\infty,t)=0, \qquad n(y,t<0)=0 \qquad n(y,0)=n_0e^{-\alpha y} \qquad 5.12$$

$$\frac{\partial n}{\partial y}_{y=0}=\frac{s}{D}n_{y=0} \qquad 5.13$$

where τ is the bulk recombination rate, μ is the carrier mobility, D is the ambipolar diffusion coefficient, E is the applied electric field,

and s is the surface recombination velocity. We assume that n is uniform in the x and z directions. Since the light pulse has a duration of 1-2 picoseconds, and since the resulting photocarriers relax from the high energy levels of the appropriate band to the low level of the band within a few (subpicosecond) collision times, we are justified in treating the carrier generation as a delta function in time. We have also assumed charge neutrality for ambipolar diffusion [12].

We begin the solution of Equation 5.11 by observing that the term n/τ may be temporarily eliminated if the final result is multiplied by $e^{-t/\tau}$. We then perform a Laplace transform on the remaining expression. We obtain

$$n_0 e^{-\alpha y} + q n(y,q) = \frac{\partial^2 n(y,q)}{\partial y^2} \qquad 5.14$$

where q is the Laplace transform variable, conjugate to the "time" variable Dt. The homogeneous solution to Equation 5.14 is

$$n(y,q) = A(q) e^{\sqrt{q}y} + B(q) e^{-\sqrt{q}y} \qquad 5.15$$

where only the second term satisfies the boundary condition at $y=\infty$, hence, A(q)=0. The particular solution of Equation 5.14 is

$$n(y,q) = C e^{-\alpha y} \qquad 5.16$$

where

$$C=\frac{n_0}{\alpha^2-q} \qquad 5.17$$

Thus, the solution is

$$n(y,q)=\frac{n_0 e^{-\alpha y}}{\alpha^2-q}+B(q)e^{-\sqrt{q}y} \qquad 5.18$$

Inserting Equation 5.18 into the surface boundary condition Equation 5.13, we obtain an expression for B(q):

$$B(q)=\frac{-n_0(\alpha+\gamma)}{(\alpha^2-q)(\gamma+\sqrt{q})} \qquad 5.19$$

where $\gamma=s/D$. In order to find n(y,t), we perform the inverse Laplace transform

$$n(y,t)=\frac{1}{2\pi i}\int_{-i\infty}^{i\infty}\left(\frac{n_0 e^{-\alpha y}}{\alpha^2-q}-\frac{n_0(\alpha+\gamma)}{(\alpha^2-q)(\gamma+\sqrt{q})}e^{-\sqrt{q}y}\right)e^{Dtq}\,dq \qquad 5.20$$

This expression has a removable singularity at $q=\alpha^2$, and no other singularities on the single sheet of the complex plane. We choose a branch cut on the negative axis, and choose the square roots to be positive imaginary above the cut, and negative imaginary below the cut. The only contribution to the contour integral is from the two paths above and below the branch cut. We obtain

$$n(y,t)=\frac{-1}{2\pi i}\int_0^{\infty}\frac{n_0(\alpha+\gamma)e^{-z^2Dt}}{\alpha^2+z^2}\left(\frac{e^{-izy}}{\gamma+iz}-\frac{e^{izy}}{\gamma-iz}\right)2z\,dz \qquad 5.21$$

where we have introduced the variable $z^2=-q$. Equation 5.21 be-

comes

5.22

$$n(y,t)=\frac{-2n_0}{(\gamma-\alpha)\pi}\int_0^{\infty}e^{-z^2Dt}\,(z\cos zy+\gamma\sin zy)\left\{\frac{1}{\alpha^2+z^2}-\frac{1}{\gamma^2+z^2}\right\}dz$$

The four terms in this integral are found in Reference [26]; simplifying, and including the term $exp(-t/\tau)$, we obtain

$$n(y,t)=n(0,0)\exp(-t/\tau-\frac{y^2}{4Dt})\left\{W(\alpha\sqrt{Dt}-\frac{y}{2\sqrt{Dt}})+W(\alpha\sqrt{Dt}+\frac{y}{2\sqrt{Dt}})\right.$$

$$\left.-\frac{2\gamma}{\gamma-\alpha}\left[W(\alpha\sqrt{Dt}+\frac{y}{2\sqrt{Dt}})-W(\gamma\sqrt{Dt}+\frac{y}{2\sqrt{Dt}})\right]\right\} \qquad 5.23$$

where γ is s/D and $W(x)=exp(x^2)erfc(x)$. Curves of Equation 5.23 are shown in Figure 5.2.

The total current passing through the carrier field described above is

$$i(t)=e\mu Ew\int_0^{\infty}n(y,t)dy \qquad 5.24$$

where w is the width of the stripline. This integral is

$$i(t)=e\mu Ewn(0,0)exp(-t/\tau)\left\{\frac{\gamma W(\alpha\sqrt{\alpha t})-\alpha W(\gamma\sqrt{\alpha t})}{\alpha(\alpha-\gamma)}\right\} \qquad 5.25$$

n(0,0) is related to the illumination level, and is

$$n(0,0)=\frac{\alpha N}{Area_{gap}}=\frac{2\eta\alpha\Phi}{Area_{pulse}} \qquad 5.26$$

Φ is the number of photons in the optical pulse, $N=2\Phi\frac{Area_{gap}}{Area_{pulse}}$ is the

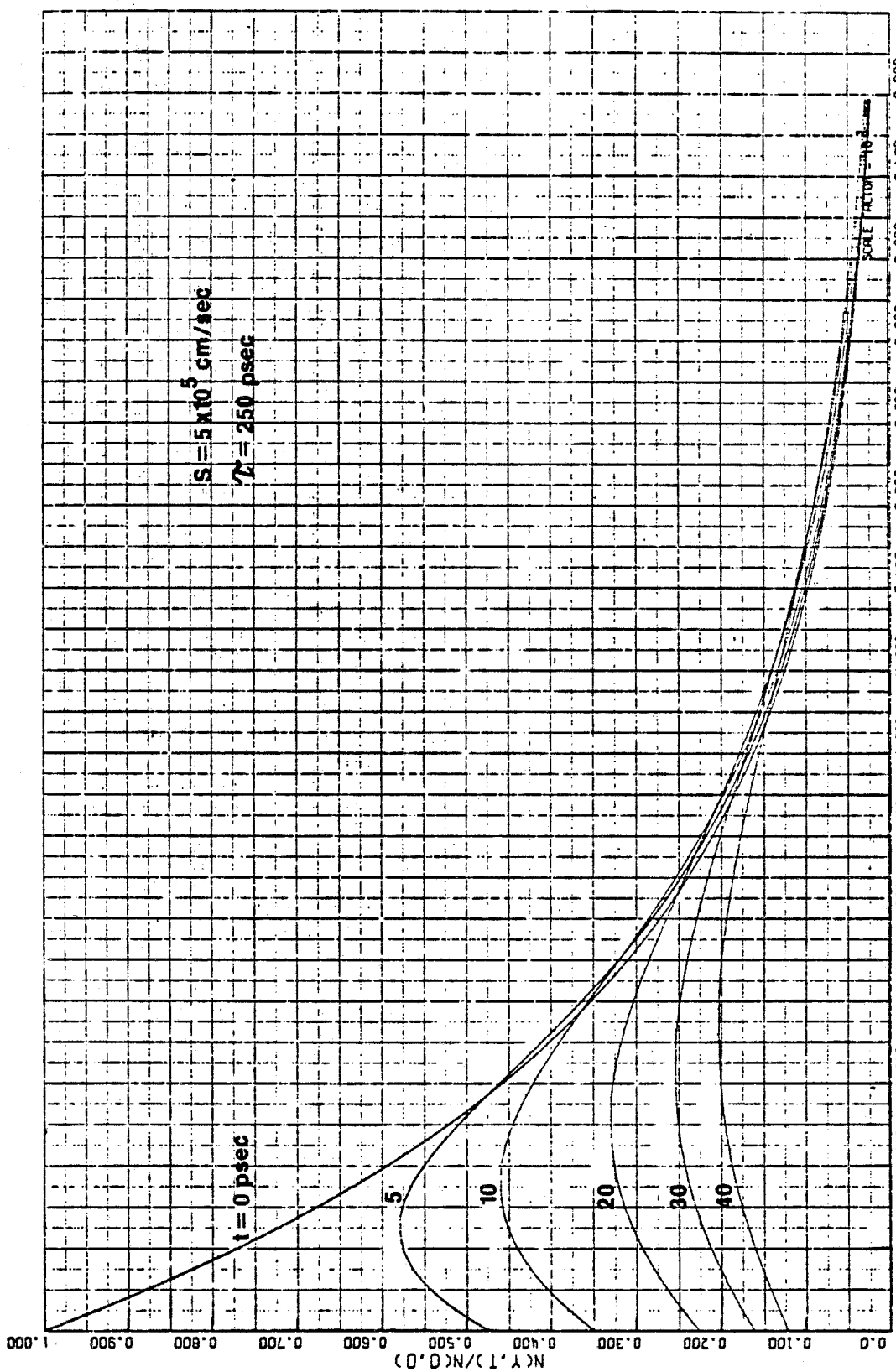

Figure 5.2 Carrier concentration as a function of time and distance into the medium.

total number of photocarriers initially in the medium, and $1-\eta$ is the Fresnel reflectivity of the medium. The laser spot just covers the entire gap; the above expression includes this geometrical coverage of the gap by the spot. Equation 5.25 is shown in Figure 5.3, as well as a filtered Equation 5.25 that would simulate an observed signal through a finite bandwidth detection system.

We now have an expression for the ultrafast photoconductivity of Cr:GaAs. In order to relate this expression (Equation 5.25) to observed data, we filter the theoretical pulse to simulate the finite bandwidth of the detection system. Thus, we can compare the decay time generated by various carrier recombination parameters to observed decay times, and hopefully use this data to deduce the recombination parameters themselves. If typical values of surface and bulk recombination constants are inserted into Equation 5.25, there is good agreement with observed photoconductivity pulses. However, the pulse shape alone cannot uniquely determine the recombination parameters [12]. For almost any given value of surface recombination velocity, there can be found a bulk recombination rate to force agreement between theoretical and experimental data. In order to measure the parameters with any accuracy, more information must be extracted from the photoconductivity of the switches. As it turns out, magnetophotoconducivity measure-

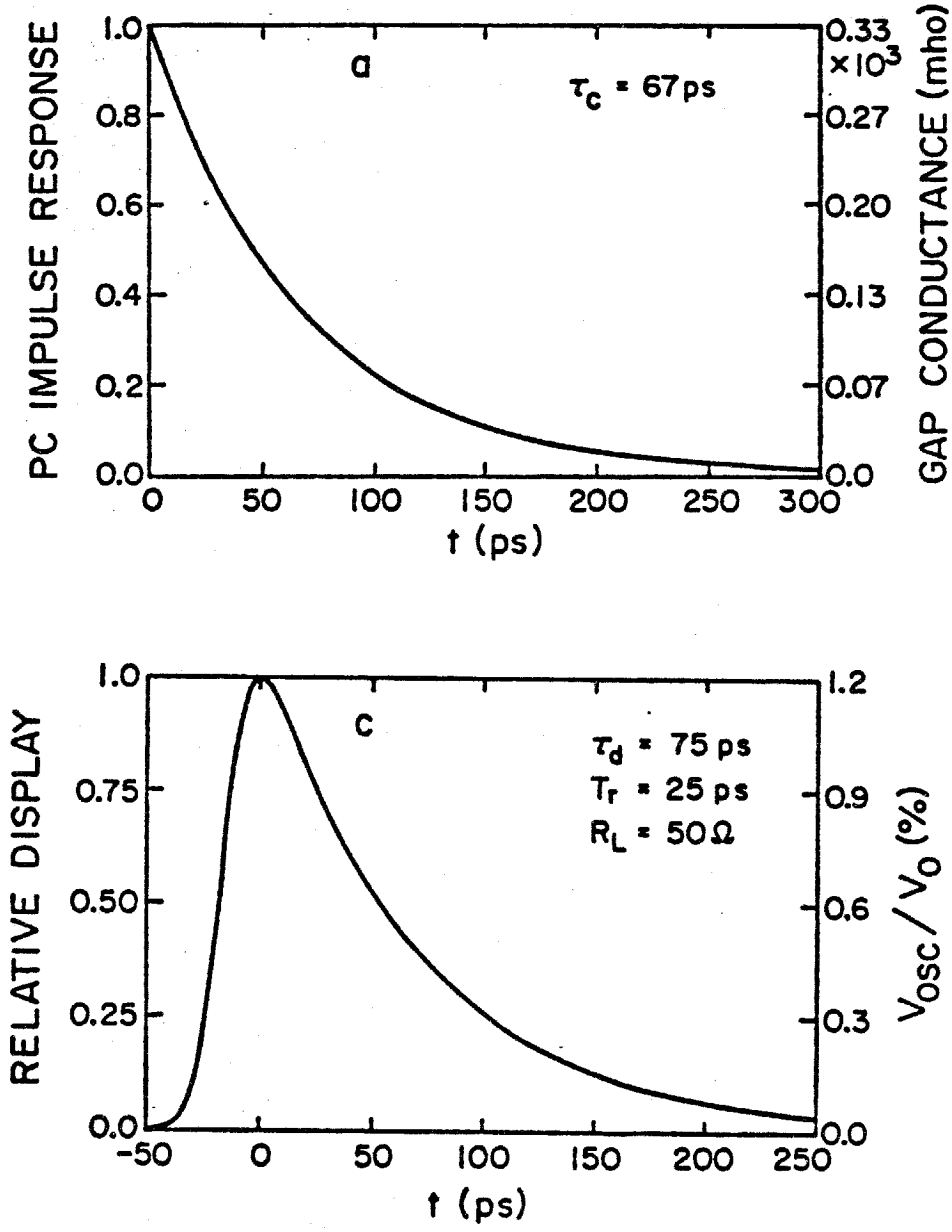

Figure 5.3 Theoretical curves of current as a function of time. The top curve is the unfiltered current, and the bottom curve is the current after passing through a Gaussian filter.

ments supply sufficient information for a reliable determination of s and τ.

Chapter 6

Recombination Parameter Determination: Ultrafast Magnetophotoconductivity of Semi-insulating Gallium Arsenide

6.0 Carrier Dynamics in a Magnetic Field

In Chapter 5, it was shown that the diffusion equation that includes the effects of surface and bulk recombinaton could explain the behavior of the photoconductive switch. However, there is a high degree of correlation between the surface and bulk recombination rates that prevail in the semiconductor. The two phenomena act in concert; in order to determine the separate recombination parameters to any degree of accuracy, the recombination processes must be decoupled in some way. This decoupling can be accomplished by applying a magnetic field perpendicular to the electric field and to the surface of the semiconductor (See Figure 6.1).

Without the magnetic field, the carriers are simply drawn to the appropriate electrode by the action of the applied electric field. When the magnetic field is applied, the electrons and holes (traveling in opposite directions and bearing opposite charges) are both impelled toward or away from the surface according to the direction of $\vec{E}\times\vec{B}$. The carriers always experience bulk recombination; when the signs of the fields are such that the carriers are

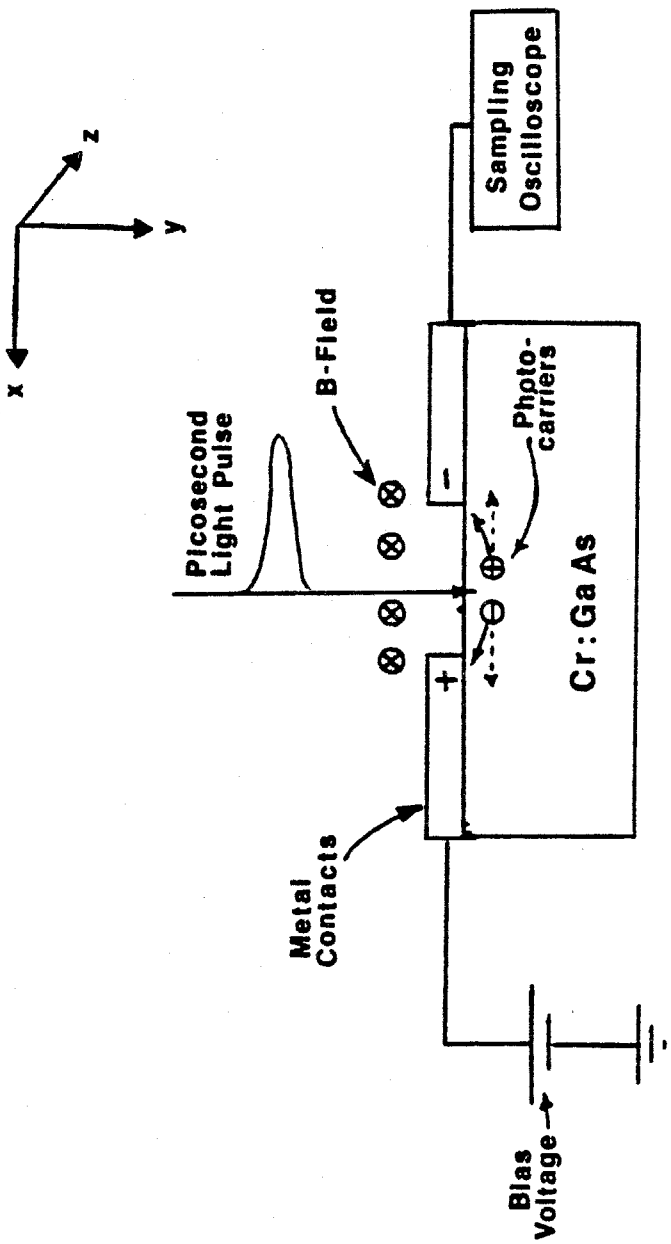

Figure 6.1 The Opto-Electronic Switch in a Magnetic Field

drawn toward the surface, more carriers experience surface recombination as well. When the fields force the carriers into the medium, fewer carriers recombine at the surface. The net result of the magnetic field is the increase or decrease of the overall lifetime of all the carriers. Thus, the observed photoconductivity trace will show an increase or decrease in pulse width, according to the signs of the fields. Such a phenomenon has been observed. This effect is known as magnetophotoconductivity (MPC). By this method, the two recombination processes can be decoupled, and the respective recombination parameters can be determined with reasonable accuracy.

Another basic photo-electric measurement undertaken in a magnetic field is the magnetophotoelectric effect (MPE). MPE measurements involve the detection of a short circuit current through the illuminated switch or a voltage across the switch in the absence of an applied electric field. The current flow arises from the average motion of carriers normal to the surface. Initially, the carriers are created at the surface; diffusion carries them into the bulk. Since both carriers are initially traveling into the bulk, the magnetic field bends the paths of electrons in one direction, and holes in the other (See Figure 6.2). Thus, a pulse of current is produced according to the direction of the magnetic field.

We derive the carrier dynamics necessary to describe the PME

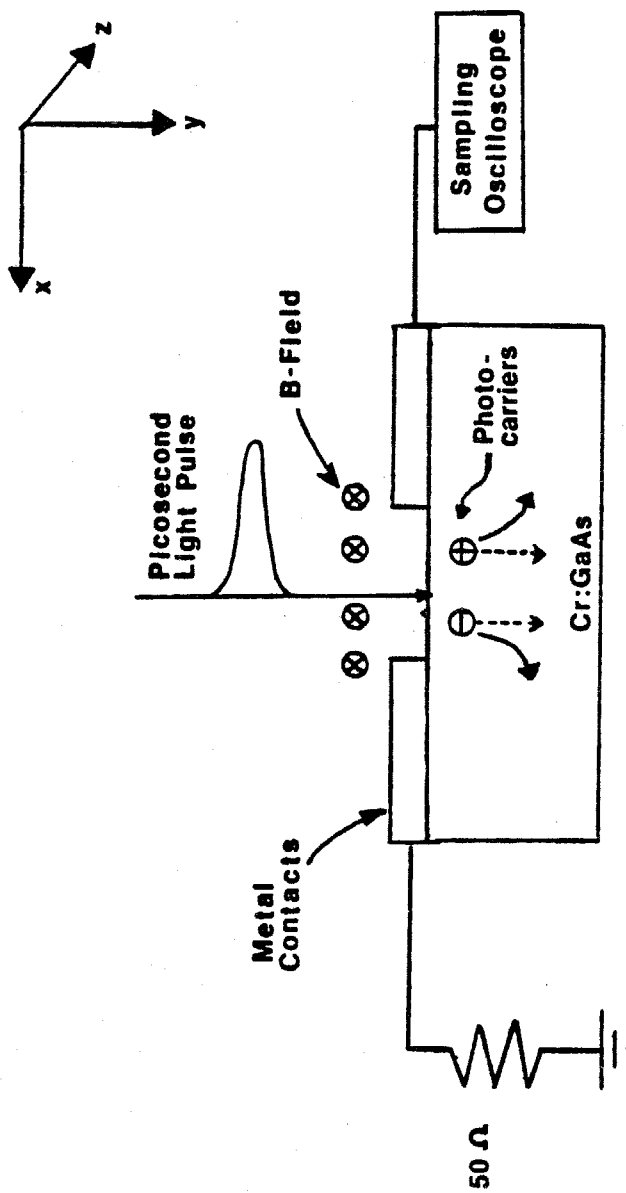

Figure 6.2 The Ultrafast Photomagnetoelectric Effect

and MPC effects by following the treatment of Beer [27a]. The current density j that arises from electric and magnetic fields is given by

$$j=\sigma_H \vec{E}^* + \alpha_H \vec{E}^* \times \vec{B} \qquad 6.1$$

where $\vec{E}^*$ is defined as

$$\vec{E}^* = \vec{E} + \nabla\xi/e \qquad 6.2$$

and where $\vec{E}$ and $\vec{B}$ are the applied electric and magnetic fields. ξ is the chemical potential, which, in the case of a classical (nondegenerate) Maxwellian semiconductor is related to particle gradients by

$$\nabla\xi = kT\frac{\nabla n}{n} \qquad 6.3$$

For sufficiently small magnetic fields, that is, for the cyclotron frequency eB/m small compared to the collision time τ, σ_H and α_H are given by

$$\sigma_H \equiv -\frac{e^2}{4\pi^3\hbar^2}\int \tau \frac{\partial \varepsilon}{\partial k_i}\frac{\partial f_0}{\partial \varepsilon} d^3k \qquad 6.4$$

$$\alpha_H \equiv -\frac{e^2}{4\pi^3\hbar^2}\int \tau \frac{\partial \varepsilon}{\partial k_i}\frac{\partial f_0}{\partial \varepsilon}\frac{e\tau}{m^*} d^3k \qquad 6.5$$

where f_0 is the carrier distribution function, τ is the collision time,

k_i is a single component of the momentum, and m^* is the effective mass of the charge carrier. We assume a Maxwellian distribution function, $f_0=e^{(\epsilon-\epsilon)/kT}$ and evaluate σ_H and α_H

$$\sigma_H=\frac{e^2\hbar^2}{12\pi^3m^{*2}kT}\int\tau f_0k^2d^3k=\frac{e^2n<\tau v^2>}{3kT} \qquad 6.6$$

$$\alpha_H=\frac{e^3\hbar^2}{12\pi^3m^{*3}kT}\int\tau^2f_0k^2d^3k=\frac{e^3n<\tau^2v^2>}{3mkT} \qquad 6.7$$

We have used the relationships $\epsilon=\hbar^2k^2/2m^*$, and $k=m^*v/\hbar$, and a Maxwellian form for f_0. The brackets <> represent an average value obtained from integrating the term within the brackets with the distribution function f_0.

We insert Equations 6.6, 6.7, and 6.2 into Equation 6.1, and obtain

$$j=\frac{ne^2<\tau v^2>\vec{E}}{3kT}+\frac{e^2\nabla n<\tau v^2>}{3}$$
$$+\frac{ne^3<\tau^2v^2>\vec{E}\times\vec{B}}{3m^*kT}+\frac{e^2<\tau^2v^2>\nabla n\times\vec{B}}{3m^*} \qquad 6.8$$

We recognize the first term in Equation 6.8 as the common expression $j=ne\mu E$, where μ is the carrier mobility. Thus, we have

$$\mu=\frac{e<\tau v^2>}{3kT} \qquad 6.9$$

The second term is the diffusion expression $j=enD\frac{\nabla n}{n}$. By compar-

ing the first two terms, we then have the Einstein relation

$$D=\frac{\mu kT}{e} \qquad 6.10$$

The third term describes a current flow in the direction of $\vec{E}\times\vec{B}$, that is, toward or away from the surface (according to the geometry specified in Figure 6.1). This is the MPC effect. The magnitude of the current density toward or away from the surface is

$$\vec{j}_{MPC}=\frac{ne^3\langle\tau^2v^2\rangle\vec{E}\times\vec{B}}{3m^*kT}=ne\,\mu\cdot\mu_H\vec{E}\times\vec{B} \qquad 6.11$$

where μ_H is the Hall mobility, defined to be [27b]

$$\mu_H=\frac{e}{m^*}\frac{\langle\tau^2v^2\rangle}{\langle\tau v^2\rangle} \qquad 6.12$$

The fourth term in Equation 6.8 involves a current perpendicular to the magnetic field and the carrier gradient, i.e., in the x-direction (See Figure 6.2). This current density is present in the absence of an electric field; it is the PME effect. Its magnitude is

$$\vec{j}_{PME}=\frac{e^2\langle\tau^2v^2\rangle\nabla n\times\vec{B}}{3m^*}=e\,\mu_H BD\,\nabla n \qquad 6.13$$

Let us compare the relative magnitudes of the photoconductive PC and PME current densities. The ratio of j_{PME} and j_{PC} is

$$\frac{j_{PME}}{j_{PC}}=\frac{e\,\mu_H BD\,\nabla n}{ne\,\mu E}=\frac{BD\,\nabla n}{nE} \qquad 6.14$$

Here, we take the conductivity mobility and Hall mobility to be equal. In our experiment, E was typically 5×10^5 v/m, and D was taken to be $8.2\times10^{-4} m^2/sec$. The initial (t=0) value of $\nabla n/n$ is $-\alpha$, the absorption coefficient; we can take this figure for an upper limit on $\nabla n/n$, since the overall gradient of the carrier distribution will decrease with time due to diffusion. The magnetic field was 15 kilogauss. Thus, the ratio of the current densities is approximately 10^{-2}. Hence, the current due to the PME effect will be small compared to conduction current due to the applied electric field. Consequently, the PME effect will only be observed when E=0.

We have derived expressions for the current density arising from the application of a magnetic field to a semiconductor. The result for the MPC effect will be included in the differential equations which relate current flow toward the surface to enhanced surface recombination. The PME current pulse that is produced upon illumination of the opto-electronic switch is directly proportional to the current density described above.

6.1 Ultrafast PME; Theory and Experiment

The PME effect under ultrafast illumination can be described in terms of the carrier concentration expression developed earlier. The result obtained above can be seen intuitively by assuming that the carriers have an average diffusion velocity in the y-direction

$$v_y = \frac{-D}{n}\frac{\partial n}{\partial y} \qquad 6.15$$

where n(y,t) is given in Equation 5.23 , and D is the ambipolar diffusion. In the presence of the magnetic field B, the carriers gain a velocity component in the x-direction

$$v_x = v_y \theta_H = v_y \mu B \qquad 6.16$$

where $\theta_H = \mu B$ is the Hall angle. Thus, the current density in the x-direction at a depth y is

$$j = e\mu B D \frac{\partial n}{\partial y} \qquad 6.17$$

which is the same result as Equation 6.13. In our analysis, we take the magnitude of the Hall mobility and the conductivity mobility to be the same; Philadelpheus and Euthymiou [28] find that the two mobilities are nearly identical in samples of Cr:GaAs with nearly equal electron and hole concentrations. We assume that during the time of observation (<100 psec), the concentrations of electrons and holes remain nearly the same. Thus, we use their result of $\mu = 3000 cm^2/v-sec$ for electron mobility, and a ratio of 20 for μ_e/μ_h. To an accuracy of five percent, then, we can ignore the contribution of holes to conduction.

The total current i passing into the contacts is the integral

$$i(t)=w\int j(y)dy=ew\mu BD\int_a^{\infty}\frac{\partial n}{\partial y}dy \qquad 6.18$$

where e is the charge of an electron, and w is the width of the contact. We integrate directly to obtain

$$i(t)=ew\mu BD\{n(0,t)-n(\infty,t)\}=ew\mu BDn(0,t) \qquad 6.19$$

or, using Equation 5.23 ,

$$i(t)=\frac{2ew\mu\eta\alpha\Phi BD}{Area_{pulse}}e^{-t/\tau}\frac{\alpha W(\alpha\sqrt{Dt})-\gamma W(\gamma\sqrt{Dt})}{\alpha-\gamma} \qquad 6.20$$

where τ is the bulk recombination lifetime, and the other constants are the same as in Chapter 5.

The PME pulse reflects only the preponderance of carrier movement into the bulk; the pulse only exists for as long as there is a preferred direction of the diffusion velocity. Since this diffusion velocity is proportional to the slope of the curves shown in Figure 5.2, the diffusion velocity ceases having that preferred direction when there is (roughly) as much of the curve n(y,t) on the left of the maximum as there is on the right. Thus, the average diffusion velocity can approach zero while there are still plenty of photocarriers present in the material. Consequently, the PME pulse is faster than the magnetophotoconductivity (MPC) pulse. It is so much faster, in fact (theoretical FWHM=5 psec), that our propagation and detection system was completely incapable of resolv-

ing any of its features. An instrument limited pulse was seen with a FWHM of 50 psec; the amplitude was low (160 microvolts across 50 ohms), and was most effectively monitored with the signal averaging system.

Since there was no method of resolving the PME pulse shape or width, the only useful data emerging from the experiment was the total charge in the current pulse. The PME pulse passed through a filtering process which presumably did not attenuate the DC component of the pulse. Thus, the integral of Equation 6.20 should match the total charge observed in the experiment.

The integral of Equation 6.20 is

$$Q_{tot}=\frac{2e\omega\mu\eta\alpha\Phi BD\tau}{Area_{pulse}(\alpha\sqrt{D\tau}+1)(\gamma\sqrt{D\tau}+1)} \qquad 6.21$$

The pulse contained $\Phi=2\times10^{6}$ photons, B was 15 kilogauss, the diffusion coefficient D is $8.2\times10^{-4} cm^2/sec$, the Fresnel reflectivity $1-\eta=\left[\frac{n-1}{n+1}\right]^2=0.32$, the absorption length $1/\alpha$ = 2300 angstroms, the mobility μ=3000 cm^2/volt-sec, and γ=s/D, where the surface recombination velocity $s=5\times10^{5}$ cm/sec. The bulk recombination rate was τ= 250 picoseconds, so the diffusion length $\sqrt{D\tau}$ was 4500 angstroms. The microstripline width w, was equal to the diameter of the laser spot, which was 2mm.

The total Q, therefore, was 1.1 x 10^{-15} coulombs. The total observed charge was 160 microvolts across 50 ohms for 50 picoseconds, which corresponds to 1.6 x 10^{-16} coulombs. Since the carriers were not forced into the contacts to be detected, many carriers simply diffused under the contacts and recombined. For those carriers that were so deep into the crystal that no replacement charge could be drawn from the contacts, a local field would build up as the charges separated that would arrest the motion of the carriers. This may account for the small observed signal.

6.2 Ultrafast MPC-Theory

The analysis of MPC parallels that of the photoconductivity derivation in Chapter 5. It is necessary to include the magnetic drift term in the diffusion equation and in the surface boundary condition that was derived in Section 6.0.

$$j_{MPC} = ne\mu^2\vec{E}\times\vec{B} \qquad 6.22$$

This expression is added to the current equation (5.10)

$$\vec{j}=-eD\nabla n+en\mu\vec{E}+ne\mu^2\vec{E}\times\vec{B} \qquad 6.23$$

(here, $\vec{E}=E\hat{\imath}$, and $\vec{B}=B\hat{k}$) and to the surface boundary condition Eqn. 5.13 at the y=0 surface

$$D\frac{\partial n}{\partial y}_{y=0}+n\mu^2EB=ns \qquad 6.24$$

We recall that the surface recombination velocity is the ratio of carriers that recombine per unit time and area to the surface carrier concentration. The right hand side of Equation 6.24 is this rate of carrier recombination per unit time and area. This must be equal to the number of carriers that arrive at the surface per unit time and area, which is given by the sum of the diffusion current and the magnetic drift.

The continuity equation remains the same as Equation 5.9 ,

$$\frac{\partial n}{\partial t}=-\nabla\cdot\vec{j}-\frac{n}{\tau} \qquad 6.25$$

and the other boundary conditions are unchanged as well. Assuming that n is constant in the x and z directions, the resulting differential equation is

$$\frac{\partial n}{\partial t}=D\frac{\partial^2 n}{\partial y^2}+2Dk\frac{\partial n}{\partial y}-\frac{n}{\tau} \qquad 6.26$$

where

$$k=\frac{\mu^2EB}{2D} \qquad 6.27$$

The solution of Equation 6.26 is related to the B=0 solution in a straightforward manner [29]. Assume that a function h(y,t)

satisfies the B=0 differential equation and boundary conditions, Equations 5.11-5.13. h(y,t) will be equal to Equation 5.23. Now consider a function n(y,t), such that

$$n(y,t)=e^{-k(y+Dkt)}h(y,t,\alpha\rightarrow\alpha-k,\gamma\rightarrow\gamma-k) \qquad 6.28$$

where the constants α and γ are replaced with $\alpha-k$ and $\gamma-k$, as indicated. We will now show that the function n(y,t) as defined in Equation 6.28 is a solution to the differential equation (Equation 6.26) and its boundary conditions. First, we note that the presence of the term $\frac{-n}{\tau}$ in Equation 6.26 merely introduces a factor $e^{-t/\tau}$ in the result; since both differential equations have this term, we need not carry it through the derivation of n(y,t). Inserting Equation 6.28 into Equation 6.26, we obtain

$$\frac{\partial h}{\partial t}-Dk^2h=D\left[\frac{\partial^2 h}{\partial y^2}-2k\frac{\partial h}{\partial y}+k^2h\right]+2Dk\frac{\partial h}{\partial y}-2Dk^2h \qquad 6.29$$

Using our assumption that h(y,t) satisfies Equation 5.11, we see that the equality in Equation 6.29 holds. Now we must verify that n(y,t) in Equation 6.26 satisfies the boundary conditions.

First, we show that $n(\infty,t)=0$. Since the B=0 carrier concentration decreases at least as fast as $e^{-y^2/4Dt}$ according to Equation 5.23, then, regardless of the sign of k in the exponential in Equation 6.28, n(y,t) will always vanish for sufficiently large y.

The initial profile of h at t=0 is $n_0 e^{-\alpha y}$. We substitute $\alpha - k$ for α, and see that

$$n(y, 0) = e^{-ky} h(y, 0) = n_0 e^{(-k-(\alpha-k))y} = n_0 e^{-\alpha y} \qquad 6.30$$

Thus, the t=0 initial condition is satisfied. Since h=0 for t less than zero, n will be zero prior to illumination as well.

The last boundary condition is the surface recombination expression Equation 6.24. We rewrite Equation 6.24 in terms of k and $\gamma = s/D$

$$\frac{1}{n}\frac{\partial n}{\partial y}_{y=0} = \gamma - 2k \qquad 6.31$$

Inserting Equation 6.28 into 6.24, we obtain

$$-k + \frac{1}{h}\frac{\partial h}{\partial y}_{y=0} = \gamma - 2k \qquad 6.32$$

Since h satisfies the surface boundary condition, we may replace $\frac{1}{h}\frac{\partial h}{\partial y}$ with $\gamma - k$, and observe that the boundary condition is satisfied. Hence, the relationship between the B=0 case and the MPC effect stated in Equation 6.28 is valid.

The function n(y,t) taken from Equation 6.28 is shown graphically in Figure 6.3 as a function of the distance into the material with the time t as a parameter. The three sets of curves show the carrier concentration profile at successive times under a magnetic

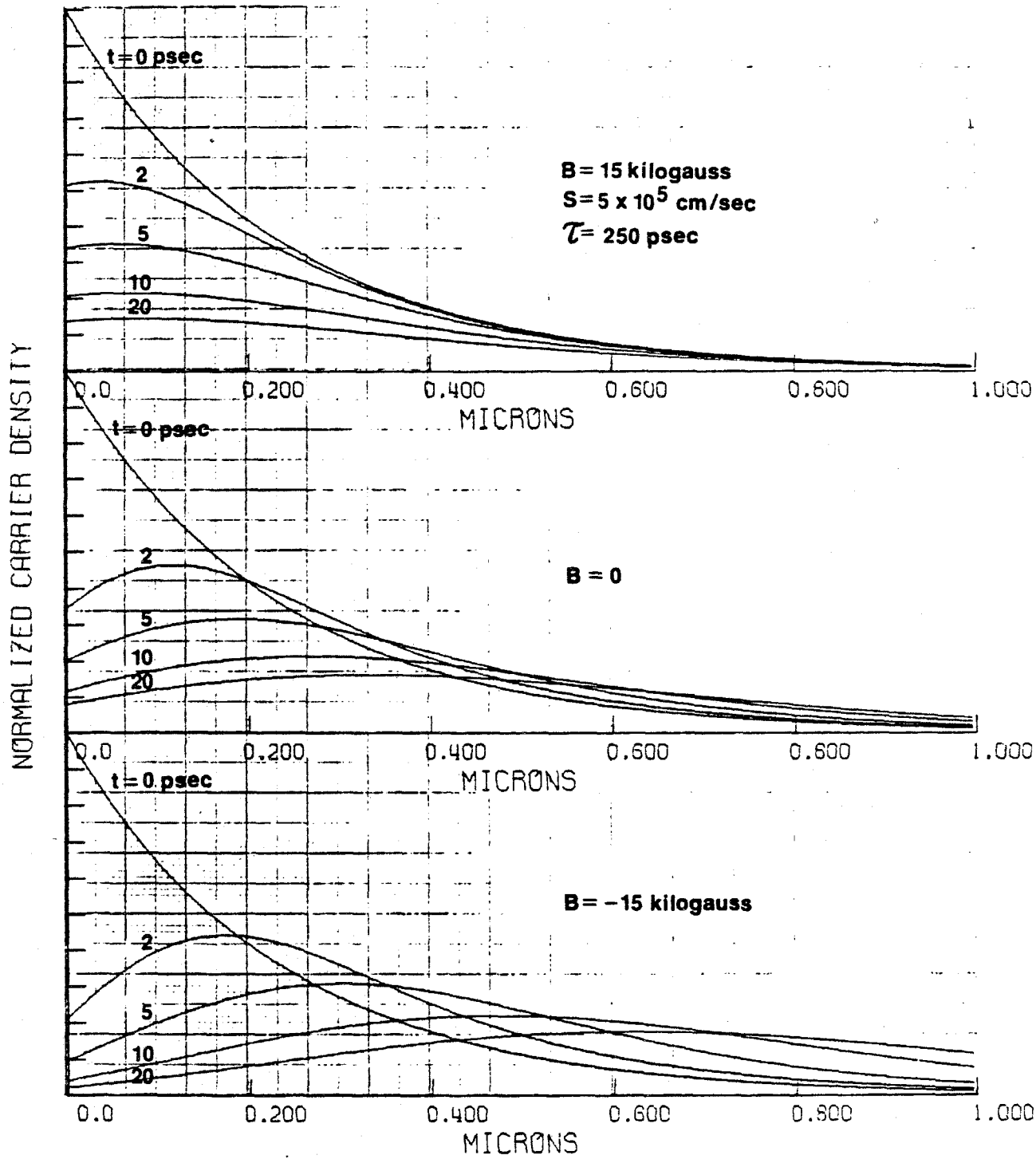

Figure 6.3 Theoretical curves of carrier concentration as a function of time, distance into the medium, and applied magnetic field.

field B=15kgauss, B=0, and B=-15kgauss. The geometry is such that the carriers are impelled toward the surface for positive B, and pushed into the bulk for negative B. It is clear that the surface recombination rate, which is proportional to $s \cdot n(0,t)$, is greatest in the top curves, and least in the bottom curves. In fact, since n(0,t) is drawn almost immediately to zero in the bottom trace, the surface recombination is almost completely suppressed. The condition for suppression of surface recombination is $Dk >> D\gamma$, that is, the magnetic drift velocity must be much greater than the surface recombination velocity. Thus, the B-field must be much greater than $\frac{2s}{\mu^2 E}$. In our experiment, this condition was satisfied if the B-field greatly exceeded 12 kgauss. Since we used 15 kgauss, the surface recombination was not entirely suppressed; however, the data obtained in a negative B-field closely approximated the character of a s=0 measurement.

The data obtained from photoconductivity tests is sensitive to the total charge present in the material. Thus, the current pulse will be proportional to the integral of the charge distribution:

$$i(t) = we\mu E \int_0^\infty n(y,t)\,dy \qquad 6.33$$

where w is the stripline width, and n(y,t) is the carrier concentration under the influence of the magnetic field. Performing the integral, we obtain

$$6.34 \qquad i(t)=\frac{2we\mu E\eta\Phi e^{-t/\tau-Dk^2t}}{Area_{pulse}}\left\{\frac{k(\alpha^2-\gamma^2)W_k+\alpha(\gamma^2-k^2)W_\alpha+\gamma(k^2-\alpha^2)W_\gamma}{(\alpha-k)(k-\gamma)(\gamma-\alpha)}\right\}$$

where $W_i=W(i\sqrt{Dt})$, with $W(x)$ defined above, and where the above substitutions for α and γ must be performed. Plots of Equation 6.34 are shown in Figure 6.4. Shown are curves of current versus time; this would be the output of an infinitely fast oscilloscope. Actual data will reflect the finite bandwidth of the transmission and detection system. Since the carriers experience enhanced recombination when they are forced to the surface, a B-field of the proper sign will decrease the width of the current pulse, and vice versa. The effect of the finite bandwidth of the detection system will be to reduce the apparent height of the narrow pulse as well.

6.3 Ultrafast MPC-Experiment

The MPC data was obtained by repeating the photoconductivity experiments in the presence of a magnetic field. Special pole faces were constructed for the magnet in order to maximize the field in the region of the GaAs chip. The separation of the conical pole faces was 2mm (the width of the chip), and clearance for the microstripline was cut into the pole faces. This maximized the local B-field at the chip, and minimized the impedance contribution from the grounded metal pole faces. The magnet drew 10 amperes at 100 volts, and produced 15kgauss at the location of the chip as measured with a gaussmeter.

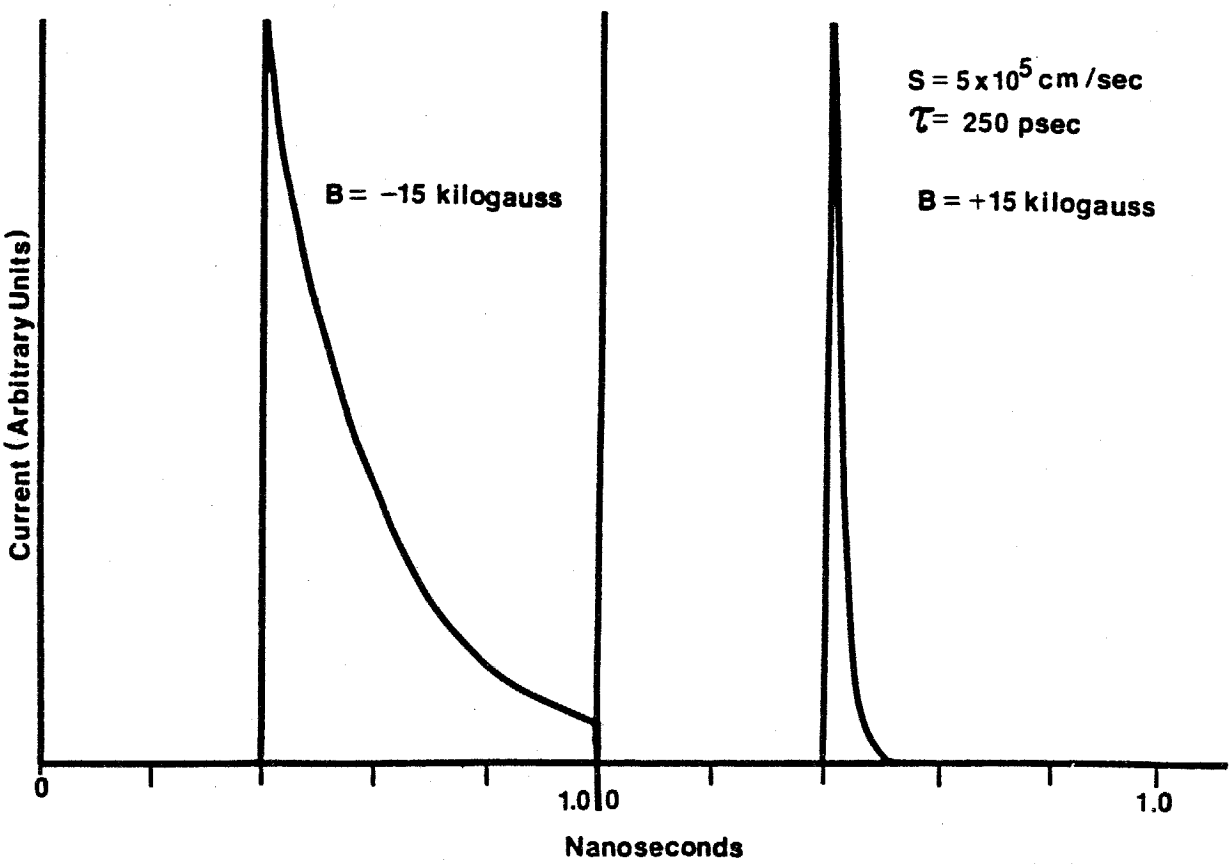

Figure 6.4 Theoretical curves of current as a function of time and magnetic field

Early measurements involved storing several separate photoconductivity traces on magnetic tape. Each trace represented data obtained using different magnetic field intensities, and each was the average of several seconds of sampling oscilloscope sweeps. The dye laser pulse amplitude, however, did not always remain stable over the time necessary to acquire the several traces. As a result, the first traces were inconsistent with the last traces.

A means of data acquisition was devised that was insensitive to dye laser fluctuations. Since it is the product EB that determines the nature of the magnetic effect, it was decided that the magnetic field be kept constant, and the electric field (the voltage across the gap) switched rapidly from one polarity to the other. Rapid switching of the magnetic field was deemed impractical. A routing circuit was devised which passed the positive E-field photoconductivity pulse trace to one half of the memory of the signal averager, and inverted and passed the negative data to the other half of the memory. Thus, two traces were simultaneously stored into memory, one demonstrating the effect of carriers driven into the bulk of the semiconductor, and the other showing enhanced surface recombination. The amplitude was recorded with 12-bit resolution, and the sweep was digitized to a density of four channels per picosecond. This data was written onto magnetic tape to be processed on a computer. Each sample was previously tested to

verify that it was isotropic to current flow in either direction in order to ensure accurate interpretation of the data.

The FORTRAN program used to analyze the data read a record from the tape and smoothed, normalized and sampled the data into a 128 element array. Another array was generated using Equation 6.34 . This analytical array was filtered with a Gaussian filter having a bandwidth associated with a risetime of 30 picoseconds (the risetime of the detection system). The filtered array was compared to the experimental data by means of a least-squares nonlinear parameter curve fitting routine. The adjustable parameters given to the fitting routine were the vertical scale, the horizontal position, the bulk recombination rate, and the surface recombination velocity. The results of such calculations are shown in Figure 6.5 and 6.6 for switches of different surface preparations; the solid lines are the experimental data, the symbols indicate the analytical curves.

It is clear that the magnetic field increases or decreases the overall lifetime of the carriers. We see in Figure 6.5 that the width of the first pulse is approximately double that of the second pulse. The height difference is a result of the finite speed of the detection system; both pulses have the same initial amplitude at the gap, but the narrower pulse is more broadened and reduced in height due to the attenuation of its high frequency components.

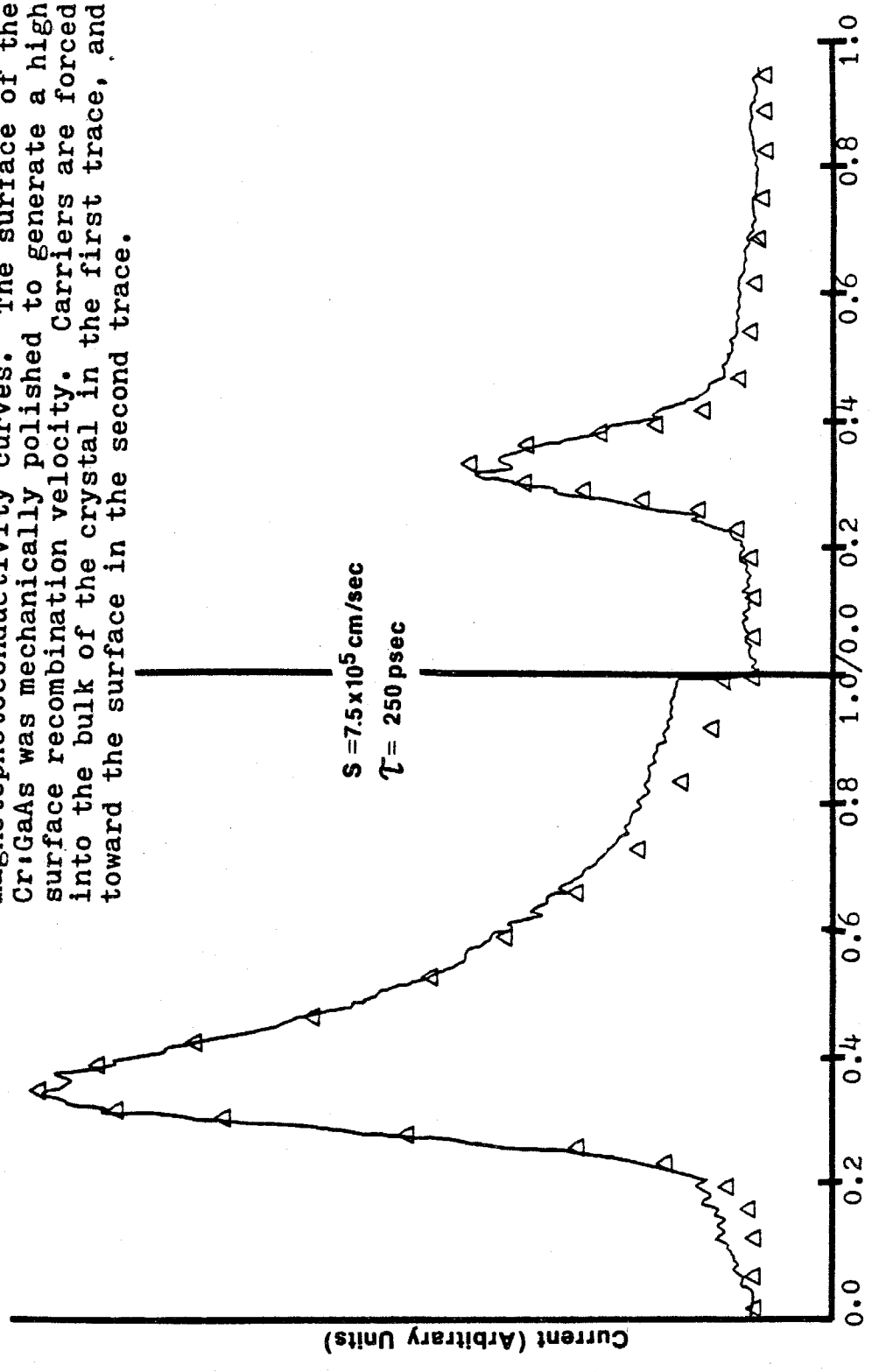

Figure 6.5 Experimental (solid curve) and theoretical (symbols) magnetophotoconductivity curves. The surface of the Cr:GaAs was mechanically polished to generate a high surface recombination velocity. Carriers are forced into the bulk of the crystal in the first trace, and toward the surface in the second trace.

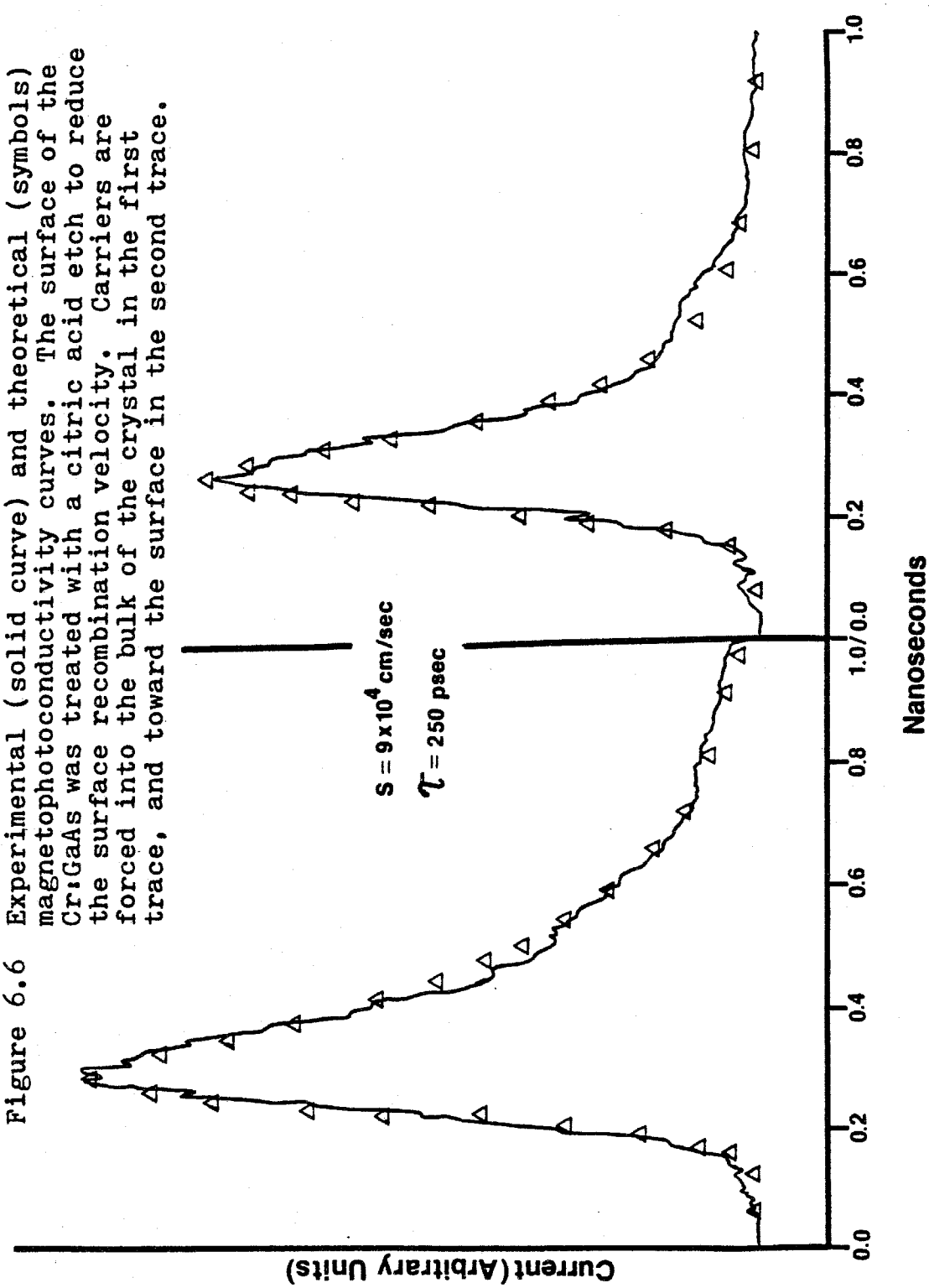

Figure 6.6 Experimental (solid curve) and theoretical (symbols) magnetophotoconductivity curves. The surface of the Cr:GaAs was treated with a citric acid etch to reduce the surface recombination velocity. Carriers are forced into the bulk of the crystal in the first trace, and toward the surface in the second trace.

6.4 Summary of the Experimental Results

We see that the fit between the theoretical and experimental curves is very good, and, equally as important, the fit is inflexible to variations of s and τ. Without the magnetic field, the parameters were extablished to within an accuracy of an order of magnitude for τ, and to many orders of magnitude for s [12]. The magnetic field nearly eliminated this flexibility of the fitting process, and determined both parameters such that a satisfactory fit was obtained only within a range of ten percent of the parameters. This range was found by providing the fitting program with a wide variety of initial estimates for s and τ. Regardless of the initial estimates, the final best-fit parameters fell within a ten percent range.

The parameters returned from the fitting routine compare favorably with material parameters determined by other investigators. The bulk recombination rate was quite uniform over the collection of switches tested; τ was determined to be 250±50 picoseconds. Our value of τ agrees well with CW photoconductivity measurements taken under high illumination intensity (τ=250 psec. [30]). Lower intensity CW measurements show longer lifetimes (many nanoseconds) due to the presence of traps in the material with long occupation times [30-32]. A trap can be regarded as a recombination center with a higher probability of thermal emission of a captured electron (or hole) than ionized capture of a

hole (or electron). Thus, a trap will extend the lifetime of one species of carrier by isolating it from recombination with the other species. The higher the concentration of traps, the greater this lifetime extension [33]. Under high level optical excitation, there will be a sufficient number of free carriers to populate all the traps without depletion of the free carrier supply. Hence, the free carrier lifetime will be unaffected by the presence of the traps. Under δ -function illumination, the occupation of these long-lived trap states is negligible for the hundred picoseconds of observation, so our good agreement with the high intensity measurements is expected.

The surface recombination velocity was calculated to be from 8×10^4 cm/sec at a surface passivated with a citric acid etch [16] (See Figure 6.6), to 7.5×10^5 cm/sec at a mechanically polished surface (See Figure 6.5). These values are in good agreement with luminescence studies which determined s to be 5×10^4 and 10^6 cm/sec, for the respective surface preparations. We saw no magnetic field effects for the GaAlAs switch; this observation was consistent with theoretical predictions using the established value of s at the heterostructure interface. Hence, that switch reflected the recombination activity of the bulk and not the surface.

We have seen that the fast photoconductivity of Cr:GaAs can be explained with a model of carrier dynamics that involves surface

and bulk recombination processes. However, the uncertainty in determining recombination parameters through ultrafast photoconductivity alone can be as high as several orders of magnitude. The combination of a high surface recombination velocity and low bulk rate may yield photoconductivity pulses indistinguishable from those produced by a low surface rate and a high bulk recombination rate. The introduction of the magnetic field reduces this uncertainty for a single device to approximately 10%. There is a measure of the degree of correlation between two parameters that is used in nonlinear parameter fitting. This correlation coefficient (an element of a matrix in numerical analysis commonly called "r") ranges between 1 and -1, with the extreme values designating high correlation and with 0 indicating complete lack of correlation [34]. When the fitting routine is performed on a single pulse, the correlation coefficient between the surface and bulk parameters is 0.96. When two pulses obtained under different magnetic fields are treated simultaneously by the routine, the coefficient drops to 0.16. This indicates the dramatic improvement in parameter estimation when the ultrafast photoconductivity of a material is studied in a magnetic field.

Thus, the technique of ultrafast magnetophotoconductivity is a useful new tool for the succesful determination of recombination parameters in semiconductors. Recent advences in mode locked

dye laser technology, such as broadband tunability and Gigawatt output pulse powers, will enable an expansion of this diagnostic method to a wider range of materials to learn more about carrier recombination phenomena on a picosecond time scale.

References for Part II

1. C. H. Lee, A. Antonetti, and G. Mourou, Opt. Commun. 21, 158 (1977).
2. R. A. Lawton and A. Scavannec, Electron. Lett. 11, 74 (1975).
3. G. Mourou and W. Knox, Appl. Phys. Lett. 35, 492 (1979).
4. P. Lefur and D. H. Auston, Appl. Phys. Lett. 28, 21 (1976).
5. Omni-Spectra Corporation.
6. Custom Poly C, 3M Corporation.
7. G. H. McCall, Rev. Sci. Instrum. 43, 865 (1972).
8. A. H. Kwon, Microwave Journal, p. 6 (Jan. 1976).
9. E. O. Hammerstad, Proc. Europ. Micro. Conf., Hamburg, Germany, Sept. 1975, p. 268.
10. M. V. Schneider, Bell Syst. Tech. J. 48, 1421 (1969).
11. H. R. Kaupp, IEEE Trans. Electronic Computers EC-16, 185 (1967).
12. P. Agmon, Ph.D. Thesis, California Institute of Technology, 1980.
13. W. J. Getsinger, IEEE Trans. MTT-21, 34 (1973).
14. R. A. Pucel, D. J. Masse, and C. P. Hertwing, IEEE Trans. MTT-16, 342 and 1064 (1968).
15. M. V. Schneider, Bell Syst. Tech. J. 48, 2325 (1969).
16. G. P. Peka and L. P. Shepel, Sov. Phys. Solid State 14, 2025 (1973).
17. R. J. Nelson, et al., Appl. Phys. Lett. 26, 76 (1980).
18. I. Ury, private communication.
19. Al Cho grew the GaAlAs to our specifications at Bell Laboratories.
20. K. Kitahara, et al., J. Appl. Phys. 50, 5339 (1979).
21. Crystal Specialties, Monrovia, CA.
22. R. Dingle and K. F. Ridgers, Jr., Appl. Phys. Lett. 14, 183 (1969).
23. G. M. Martin, et al., J. Appl. Phys. 50, 467 (1979).

24. W. Plessiewicz, J. Phys. Chem. Solids 38, 1079 (1977).

25. W. Shockley, Phys. Rev. 56, 317 (1939).

26. I. Gradshteyn and I. Ryzhik, Table of Integrals, Series, and Products (Academic Press, New York, 1965), p. 497.

27. A. C. Beer, Solid State Physics, Supp. 4 (Academic Press, New York, 1963), a) p. 35; b) p. 101.

28. A. Philadelpheus and P. Euthymiou, J. Appl. Phys. 45, 955 (1974).

29. T. Koch and R. Moyer, unpublished.

30. S. S. Li and C. I. Huang, J. Appl. Phys. 43, 1757 (1972).

31. H. Milner-Brown and E. Fortin, Can. J. Phys. 47, 2789 (1969).

32. A. L. Lin and R. H. Bube, J. Appl. Phys. 47, 1859 (1976).

33. A. Rose, Concepts in Photoconductivity and Allied Problems (Interscience Publishers, John Wiley and Sons, New York, 1963), p. 20.

34. D. W. Marquardt, J. Soc. Indust. Appl. Math., 11, 431 (1963).